



**Design and
characterization of
specMACS**

F. Ewald et al.

This discussion paper is/has been under review for the journal Atmospheric Measurement Techniques (AMT). Please refer to the corresponding final paper in AMT if available.

Design and characterization of specMACS, a multipurpose hyperspectral cloud and sky imager

F. Ewald^{1,*}, T. Kölling^{1,*}, A. Baumgartner², T. Zinner¹, and B. Mayer¹

¹Ludwig Maximilians Universität, Institut für Meteorologie, Munich, Germany

²Deutsches Zentrum für Luft und Raumfahrt, Institut für Methodik der Fernerkundung, Oberpfaffenhofen, Germany

*These authors contributed equally to this work.

Received: 7 August 2015 – Accepted: 29 August 2015 – Published: 22 September 2015

Correspondence to: T. Zinner (tobias.zinner@lmu.de)

Published by Copernicus Publications on behalf of the European Geosciences Union.

Title Page

Abstract

Introduction

Conclusions

References

Tables

Figures



Back

Close

Full Screen / Esc

Printer-friendly Version

Interactive Discussion



Abstract

The new spectrometer of the Munich Aerosol Cloud Scanner (specMACS) is a multipurpose hyperspectral cloud and sky imager designated, but not limited to investigations of cloud-aerosol interactions in Earth's atmosphere. Equipped with a high spectral and spatial resolution, the instrument is designed to measure solar radiation in the visible and short-wave infrared region that is reflected from, or transmitted through clouds and aerosol layers. It is based on two hyperspectral line cameras that measure in the solar spectral range between 400–2500 nm with a spectral bandwidth between 2.5–12.0 nm. The instrument was already operated in ground-based campaigns as well as aboard the German High Altitude LOng Range (HALO) research aircraft, e.g. during the ACRIDICON-CHUVA campaign in Brazil during summer 2014.

This paper describes the specMACS instrument hardware and software design and characterizes the instrument performance. During the laboratory characterization of the instrument the radiometric response as well as the spatial and spectral performance was assessed. Since the instrument is primarily intended for retrievals of atmospheric quantities by inversion of radiative models using measured radiances, a focus is placed on the determination of its radiometric response. Radiometric characterization was possible for both spectrometers with an absolute accuracy of 3% at their respective central wavelength regions. First measurements are presented which demonstrate the application possibilities and show that the key demands on radiometric and spectral accuracy as posed by the intended remote sensing techniques are fulfilled.

1 Introduction

The spectrally resolved measurement of solar radiation is a long standing method in earth science. In the beginning half of the 20th century Gordon Dobson introduced the method of spectroscopy into the field of atmospheric remote sensing. On the basis of passive measurements of the absorption of solar radiation by stratospheric ozone he

AMTD

8, 9853–9925, 2015

Design and characterization of specMACS

F. Ewald et al.

Title Page

Abstract

Introduction

Conclusions

References

Tables

Figures



Back

Close

Full Screen / Esc

Printer-friendly Version

Interactive Discussion



Design and characterization of specMACS

F. Ewald et al.

Title Page

Abstract

Introduction

Conclusions

References

Tables

Figures



Back

Close

Full Screen / Esc

Printer-friendly Version

Interactive Discussion



determined the depth and variability of the ozone layer. Since then the exploitation of atmospheric absorption to measure the concentration of atmospheric constituents has led to the development of spaceborne measurement platforms like the Infrared Atmospheric Sounding Interferometer (IASI) and the Cross-track Infrared Sounder (CrIS) for spectral remote sensing of temperature and trace gas profiles.

Remote sensing of cloud and aerosol parameters is still mostly done by use of multi-spectral sensors, i.e., using only a limited number of spectral bands. Prominent examples are, e.g., ground-based aerosol retrievals using CIMEL sun-photometers in the Atmospheric Radiation Measurement Program and the Aerosol Robotic Network (AERONET) (Holben et al., 1998) or satellite based multi-channel techniques following, e.g., Hansen and Pollack (1970); Twomey and Cocks (1989) and Nakajima and King (1990) for remote sensing of cloud properties. However, the application of spectrally resolved, hyperspectral techniques in cloud and aerosol remote sensing is still in its early stages.

Systems like the Solar Spectral Flux Radiometer (SSFR, Pilewskie et al., 2003) or the Spectral Modular Airborne Radiation measurement system (SMART, Wendisch et al., 2001; Wendisch and Mayer, 2003) were used for cloud remote sensing from ground (McBride et al., 2011; Chiu et al., 2012; Jäkel et al., 2013) or airborne perspective e.g. Ehrlich et al. (2008); Eichler et al. (2009); Schmidt et al. (2007) and Coddington et al. (2010). While most techniques from these two instruments still use only a few channels to derive cloud optical thickness or cloud particle size from solar transmissivity or reflectivity measurements (Kikuchi et al., 2006; Coddington et al., 2010; McBride et al., 2011) some first techniques use spectral slopes for identification of cloud phase (Ehrlich et al., 2009; Jäkel et al., 2013). Only recently LeBlanc et al. (2015) proposed and systematically tested a range of characteristics of the full spectrum to be used for general ground-based cloud remote sensing. All of these methods are based on non-imaging sensors, i.e., only one measurement is taken at a time and one line of measurements is constructed by sensor motion or cloud motion over a ground-based measurement.

**Design and
characterization of
specMACS**

F. Ewald et al.

Title Page

Abstract

Introduction

Conclusions

References

Tables

Figures



Back

Close

Full Screen / Esc

Printer-friendly Version

Interactive Discussion



As commercially available spectral imagers for measurements in the solar visible and near-infrared spectrum become more and more affordable they become more frequently used nowadays. For airborne remote sensing of land surfaces a few, still costly commercial solutions are available at the moment. Based on spectral off-the-shelf camera systems, very similar to core sensors used in these solutions, the Meteorological Institute of the University of Munich decided to tailor a system to its specific needs. In the following this new hyperspectral imaging instrument for atmospheric measurements on ground-based and airborne platforms with a spectral coverage of 400–2500 nm will be introduced and characterized in detail. On the basis of some first applications the scientific data obtained with the specMACS instrument will be introduced.

The institute already hosts a range of instruments for remote measurements of the atmosphere: an aerosol lidar, a millimeter-wave cloud radar, a sun-photometer and multiple Differential Optical Absorption Spectroscopy (DOAS) instruments. Using this active and passive instrumentation, improvements of our understanding of the aerosol-cloud interaction in the atmosphere is pursued. Cloud microphysical development like droplet growth, glaciation processes, ice nucleation as well as cloud dynamics are influenced by the abundance and type of available cloud nuclei, the fraction of the aerosol background which can act as nucleus for droplet or ice particle growth. These microphysical processes are of greatest interest for the understanding of future climate development (Houghton et al., 2001).

To this end Marshak et al. (2006a); Martins et al. (2011); Zinner et al. (2008) and Ewald et al. (2013) proposed cloud side scanning measurements to observe the basically vertical development of cloud particles. To retrieve particle size and thermodynamic phase they propose to use reflected solar radiation in the near-visible to near-infrared spectral regions. This application is a core goal for the development of the new sensor. With the help of an imaging spectrometer the required spatially resolved measurements becomes possible. Especially the vertical dimension of these observations should reflect many aspects of cloud-aerosol-interaction as well as mixing of cloudy and ambient air (Martins et al., 2011; Rosenfeld et al., 2012). For the same partially

cloudy scenes, additional remote measurements of interacting aerosol characteristics (particle type, size, amount) as well as of some gaseous atmospheric components will become accessible by exploitation of the spectral image information.

1.1 Accuracy considerations

5 The complexity of cloud geometry and three-dimensional radiative effects related to it pose a great challenge to cloud side remote sensing. Various studies of Varnai and Marshak (2002); Marshak et al. (2006b) and Zinner and Mayer (2006) quantified the impact of three-dimensional radiative effects on particle size retrievals based on 1D radiation transfer simulations like Nakajima and King (1990) and found an overestimation
10 of effective radius by up to $2\ \mu\text{m}$ (Cornet et al., 2005) with a standard deviation of $1.5\ \mu\text{m}$ (Bréon and Doutriaux-Boucher, 2005). Especially for spatially high resolved cloud side measurements ($<100\text{m}$) standard deviations to the true effective radius can be 20% and more (Zinner and Mayer, 2006).

15 The proposed retrieval method by Martins et al. (2011) and Zinner et al. (2008) tries to account for this uncertainty by means of a statistical retrieval based on fully 3-D radiative transfer simulations. For optically thick liquid water clouds an uncertainty in effective radius of $2\ \mu\text{m}$ relates roughly to a radiance uncertainty of 20% at the near-infrared wavelength 2100nm used in the retrieval of (Nakajima and King, 1990). To limit the uncertainty in microphysical retrievals due to sensor characteristics well below
20 this uncertainty caused by 3-D radiative effects, we aim for an absolute radiometric calibration uncertainty of 5% or below. A systematic deviation of about 10% in radiance would, in most cases, produce an additional error for the retrieved quantities which would reach uncertainty values associated with mentioned 3-D effects.

25 Spectral accuracy requirements are not too strict for current microphysical cloud retrievals, as no sharp absorption line is evaluated. In order to exploit the different absorptions of smaller and larger cloud particles in the near infrared an spectral bandwidth and accuracy of $10\text{--}50\ \text{nm}$ is supposed to be sufficient. Nevertheless, measurements of highly resolved spectra are invaluable for the application of novel retrieval techniques

Design and characterization of specMACS

F. Ewald et al.

Title Page

Abstract

Introduction

Conclusions

References

Tables

Figures



Back

Close

Full Screen / Esc

Printer-friendly Version

Interactive Discussion



Design and characterization of specMACS

F. Ewald et al.

Title Page

Abstract

Introduction

Conclusions

References

Tables

Figures



Back

Close

Full Screen / Esc

Printer-friendly Version

Interactive Discussion



since various spectral atmospheric and soil features become exploitable. Spectrally high resolved measurement is needed, e.g., for photon path analysis using the optical depth of the oxygen A-band or for the detection of surface albedo influence on the basis of known spectral vegetation features. Conceivable use of the spectral data to estimate the oxygen A-band depth tightens spectral accuracy requirements to a few nanometer or less (Fischer and Grassl, 1991).

This work is based on previous work which developed hyperspectral instruments and their calibration. The general principle of measurement and the specific implementation of the used hyperspectral instrument was developed and described in detail by Aikio (2001). Jørgensen (2002) examined this design and described necessary steps in its calibration, potential error sources and their mitigation. The overall approach to the calibration is based on the work of Lenhard et al. (2015) and was carried out in close cooperation with the Remote Sensing Technology Institute (IMF) of the German Aerospace Center (DLR).

This paper is organized as follows: Sect. 2 first introduces the new specMACS instrument and its measurement principle. Next, all necessary technical amendments and software developments are introduced that make specMACS a versatile and accurate cloud remote sensing instrument usable for airborne push-broom applications as well as for ground-based cloud side or hemispheric scan (Sect. 3). In Sect. 4 the methods used during characterization and calibration of the instrument are introduced and described. Following in Sect. 5, detailed results of the radiometric and spectral sensor characterisation are given and discussed. Finally application examples are shown, presenting the first airborne deployment of the instrument on-board HALO, the German high-altitude long range research aircraft (Sect. 6). Cloud side measurements were collected through a customized side window of the aircraft during the Brazilian-German ACRIDICON-CHUVA campaign in autumn 2014.

2 The specMACS instrument

The spectrometer of the Munich Aerosol Cloud Scanner (specMACS) is an imaging spectrometer system for the measurement of solar radiation in the 400–2500 nm wavelength range, which is based on two hyperspectral line cameras. It is designed for remote sensing of cloud and aerosol optical properties and atmospheric trace gases. The emphasis is on the development of new ground-based retrieval methods of clouds as well as on the understanding of 3-D radiative effects in already existing retrieval methods. Key properties of the two imaging spectrometers that were determined in this work are given in Table 1. The instrument was developed at the Meteorological Institute of the Ludwig Maximilians University and is usually operated on the roof platform of the institute. A scanning setup allows to capture a two dimensional image with spectral information on every spatial pixel. This is illustrated in Fig. 2 by an exemplary hyperspectral data cube as measured with specMACS on the research aircraft HALO. While the hyperspectral line was arranged perpendicular to the scan path (across track) the scanner was used to create an image of cloud sides along track of the scan path. During this push-broom-like scan an highly resolved spectrum of reflected solar radiation was measured as shown in Fig. 2 where prominent absorption lines in this wavelength region are indicated. In the following the terms *along track* and *across track* denote directions perpendicular and parallel to the spatial line respectively.

2.1 Instrument concept

The instrument comprises two commercially available hyperspectral line spectrometers built by SPECIM (Specim Spectral Imaging Ltd., Oulu, Finland.). The measurement principle is based on the diffraction of a beam of light perpendicular to the entrance slit of the sensor as shown in Fig. 3. Both spectrometers are equipped with front optics, a transmission grating and a CMOS camera. After the light has passed through the front optics L_1 a slit beam is shaped by a narrow ($\approx 30 \mu\text{m}$) entrance slit in the image plane. This beam contains light from one spatial dimension as the second spatial dimension is

AMTD

8, 9853–9925, 2015

Design and characterization of specMACS

F. Ewald et al.

Title Page

Abstract

Introduction

Conclusions

References

Tables

Figures



Back

Close

Full Screen / Esc

Printer-friendly Version

Interactive Discussion



Design and characterization of specMACS

F. Ewald et al.

Title Page

Abstract

Introduction

Conclusions

References

Tables

Figures



Back

Close

Full Screen / Esc

Printer-friendly Version

Interactive Discussion



masked out by the slit. Before the light beam gets diffracted it is collimated by optics L_2 in front of the spectrograph. The beam is then passed through a Prism-Grating-Prism (PGP) spectrograph, which is composed of a transmission grating embedded between two prisms (P_1 and P_2). This Volume Phase Holographic (VPH) Transmission Grating is made of bichromated gelatin which contains periodical changes in the refractive index. Following Bragg's law (Bragg and Bragg, 1913),

$$m\lambda = d(\sin\alpha + \sin\beta) = 2d\sin\theta_B, \quad (1)$$

monochromatic light with wavelength λ entering the grating under angle α gets diffracted under the specific angle β . Here m is an integer and denotes the specific diffraction order while d is the grating spacing. The diffraction for wavelength λ_B is maximized when the angle of diffraction β equals the angle of incidence α , which is known as the Bragg condition. For this reason the first prism P_2 refracts the light beam at the Bragg angle θ_B onto the grating after the beam is collimated by the entrance optics of the spectrograph.

A second prism P_2 refracts the light from the $m = -1$ Bragg diffraction order back again in such a way that the light with one (central) wavelength λ_c aligns with the optical axis of the system. Nearby wavelengths get spread along the axis perpendicular to the spatial dimension of the light beam. This setup facilitates the spectral diffraction of the beam along the optical axis, which simplifies the instrument design and reduces the overall instrument size. Behind the PGP-element the beam is then focused on a second image plane by the focusing lens L_3 . In this plane an CMOS active pixel sensor (APS) (Fossum, 1997) then measures the radiant flux of the spectrally separated beam. While the spatial variations of the radiant flux are captured on one dimension its spectral variations are registered on the other dimension of the sensor. An order blocking filter (OBF) is mounted just in front of the APS to prevent spectral overlap of different diffraction orders m .

2.2 VNIR spectrometer

The spectral camera PFD (SPECIM SP-PFD-CL-65-V10E) is used for the coverage of the visible and near-infrared wavelength range (400–1000 nm) (which in the following is referred to as the visible near-infrared, VNIR). It is equipped with a 18.5 mm $f/2.4$ front lens (OLE18.5). Inside the spectrograph (ImSpector V10E) the entrance slit, the collimating optics, the PGP-element and the focusing optics are firmly connected together. Its linear dispersion is specified with 97.5 nm mm^{-1} . In front of the sensor region corresponding to longer wavelengths originating from first order $m = -1$ diffraction an order blocking filter (SPECIM OBF 570) is placed to prevent light of shorter wavelengths from second order $m = -2$ diffraction to reach the sensor. The sensor is based on a camera (MV1-D1312-160) from Photonfocus, which is built around the monochrome, uncooled CMOS active pixel sensor (A1312) from Photonfocus. This sensor is backside-illuminated to increase its low-light performance. The most important parameters are listed in Table 1.

2.3 SWIR spectrometer

For the wavelength region between 1000–2500 nm the SWIR spectrometer (SPECIM SP-SWIR-LVDS-100-N25E) is used. It is equipped with a 15 mm $f/2.1$ front optic lens (OLES15). Since the solar radiance decreases strongly from 1000 to 2500 nm the usable dynamic range over the complete wavelength range would be very limited. A spectral flattening filter (Hebo RC 01, SPECIM) is therefore placed in front of the lens to attenuate the shorter wavelengths and thereby improve the overall use of the dynamic range of the sensor for solar radiation. This filter has an additional special coating to block the wavelength range from 800–960 nm since the SWIR sensor is already sensitive from 800 nm onwards and since these wavelengths cannot be filtered by an order blocking filter. The linear dispersion of its spectrograph (ImSpector N25E) is specified with 208 nm mm^{-1} . Just like in the case of the VNIR an order blocking filter (OBF 1400) is placed in front of the SWIR sensor to prevent spectral overlap from different

Design and characterization of specMACS

F. Ewald et al.

Title Page

Abstract

Introduction

Conclusions

References

Tables

Figures



Back

Close

Full Screen / Esc

Printer-friendly Version

Interactive Discussion



diffraction orders. The SWIR spectrometer uses the MARS SW 320 × 256 sensor from SOFRADIR with a pixel pitch of 30 μm. The HgCdTe-based detector is thermoelectrically cooled to 200K to reduce the level of dark current noise. The most important parameters are listed in Table 1

2.4 Stray light protection

During zenith cloud measurements obvious signs of stray light were observed. This became clear when the front optics were temporarily shielded from light from outside the field of view, which resulted in a significant drop in measured radiance. In particular, direct solar radiation onto the unshielded front optics affected the radiometric accuracy while the stray light was hard to detect in scenes with low temporal variability. To mitigate the effects of stray light, a system of shielding baffles which are placed in front of the cameras optics (Fig. 4) was designed. The stray light protector was built of aluminium which was sandblasted, anodized and painted with NEXTEL Velvet Black paint. According to Dury et al. (2007), the regular and diffuse single scattering reflectance of this coating is typically less than 5% in the whole spectral range of both spectrometers. Simulations showed that these baffles attenuate incident light that originates from angles more than 15° outside the FOV by at least 2–3 orders of magnitude. After implementing the stray light protection, no visible evidence of stray light was found during ground measurements with the sun outside the FOV by more than 15°.

2.5 Scanning mount

For ground based measurements, specMACS is mounted on a scanning mount (MESU-OPTICS Mesu-Mount 200) with two rotating axes (vertical and horizontal). This allows the instrument to be pointed anywhere in the upper hemisphere and to perform precise and repeatable automated scans. The scanning mount is equipped with a customized closed loop motor controller (based on a ROBOTEQ Inc., SDC2130). It is equipped with an optical relative position encoder, which allows to control the full turn

Design and characterization of specMACS

F. Ewald et al.

Title Page

Abstract

Introduction

Conclusions

References

Tables

Figures



Back

Close

Full Screen / Esc

Printer-friendly Version

Interactive Discussion



of each axis in 10 000 steps resulting in a relative positioning accuracy of the angle of about two steps, which is accordingly 0.072° and thereby in the same order as the sensors IFOV (Instantaneous Field Of View). The closed loop control allows to record the actual position of the cameras reliably even if the motors are slipping, stuck or moved by hand. The scanning mount can be controlled using the newly developed acquisition control system as outlined below and includes manual control via a wireless controller and automated control using the CAMPAign ASistant (CAMPAS) software introduced in the following section.

3 Software

The specMACS hyperspectral imager is a multipurpose measurement system, which produces data at a rate of up to 300 MiBs^{-1} and which must be stored reliably on disk, even when operated continuously for hours. An important goal of the system design is further to provide a very flexible base system which can be reconfigured to various differing measurement campaign scenarios (e.g. ground based on a scanner vs. airborne use as push-broom instrument) and augmented with additional sensor information (e.g. scanning mount, temperature or position). All of this should be possible without rewriting the entire software and without the need of complex manual intervention when clouds are passing by and time is scarce. Especially for an airborne setup with limited operator availability, the system must be able to run fully autonomous even in the case of unexpected errors. These constraints led to the modular and distributed software concept as described below.

3.1 Software concept

To provide a measurement system which can be adapted to the various measurement purposes we designed a flexible and open software system design that can be adapted to various measurement scenarios easily. Although we opted for a highly modular and

Design and characterization of specMACS

F. Ewald et al.

Title Page

Abstract

Introduction

Conclusions

References

Tables

Figures



Back

Close

Full Screen / Esc

Printer-friendly Version

Interactive Discussion



distributed software concept, we still had to ensure that the system is capable of maintaining the constantly high data load as presented by the hyperspectral imagers. We decided to use ZeroMQ (Hintjens, 2010) as communication middleware, which was evaluated by CERN (Dworak et al., 2011, 2012) intensively.

The system is inspired by the actor model (Hewitt et al., 1973) and Erlang/OTP (Armstrong, 2007). For each individual task we use an independent actor (which can also be thought of as a server). Every actor communicates via various ZeroMQ sockets with other actors and is constantly monitored by a supervisor. Each actor can be written in any programming language and can be started or stopped at any time, independently of all other actors. As this design limits failures to short term interruptions of small parts of the system, it greatly improves resilience compared to previous monolithic implementations.

The main data flow can be seen in Fig. 5. Each camera has an associated grabber which receives the captured data stream. All captured data is immediately stored to disk while a reduced data stream is simultaneously extracted by several live processing units. This reduced data stream is sent to the user interface and an automated exposure control system. Without interfering with the original data stream the automated hardware control system is able to analyze and act upon incoming signals or user inputs.

3.2 Instrument automation

During ground-based scans or unsupervised airborne operation the integration time t_{int} has to be adjusted to avoid over- as well as underexposure. For this reason a control software was developed for the specMACS system which automatically sets integration time and controls dark frame measurements. Since the dark current signal of the SWIR sensor varies strongly with integration time and ambient air temperature frequent dark frame measurements are necessary.

Design and characterization of specMACS

F. Ewald et al.

Title Page

Abstract

Introduction

Conclusions

References

Tables

Figures



Back

Close

Full Screen / Esc

Printer-friendly Version

Interactive Discussion



3.2.1 Auto exposure

The main task of the auto exposure control system, setting the integration time t_{int} to an optimized value, was designed with three goals of descending importance in mind: Since clouds as the main object of interest are typically the brightest parts of a scene, overexposure is to be avoided in any case. To limit the number of distinct dark current measurements and to facilitate later data analysis, only a few discrete integration times will be used. These are indicated as $t_{\text{int}}(i)$ in the following. However, to recover from very bright scenes and to use the available dynamic range of the sensor in an optimal way, integration time should be increased after a certain time span of underexposed conditions.

In Fig. 6 the overall logic of the integration time regulation of the auto exposure software is illustrated. The logic is based on a histogram of the signal which is evaluated in real-time over all CMOS pixels. From the histogram, the 99th percentile (q_{99}) is calculated and stored for subsequent analysis. The q_{99} was chosen since it turned out to be a more stable indicator for current signal levels than the maximum value, which is sensitive to signal noise and bad pixels.

A limited set of integration times $t_{\text{int}}(i)$ were used during the aircraft measurement campaign ACRIDICON 2014: 0.5, 0.85, 1, 1.2, 1.5, 2, 3, 5, 8, 12, 18 and 25 ms. These values were chosen as a compromise between a sufficient range of values, reasonably small steps (less than a factor of 2) between integration times and the goal to have only a limited amount of distinct integration times.

The following algorithm is in principle independent of the frame rate, but was tested and optimized for 30 fps. To avoid overexposure, the 99th percentile q_{99} of the signal histogram is limited to 3/4 of the full dynamic range of the sensor in order to provide headroom for transient radiance peaks. If this limit is exceeded for more than four frames within the last 150 frames, the integration time $t_{\text{int}}(i)$ is reduced to the next allowed value $t_{\text{int}}(i-1)$. After such an overexposure protection is triggered, no increments to longer integration times are allowed during the following 1800 frames.

AMTD

8, 9853–9925, 2015

Design and characterization of specMACS

F. Ewald et al.

Title Page

Abstract

Introduction

Conclusions

References

Tables

Figures



Back

Close

Full Screen / Esc

Printer-friendly Version

Interactive Discussion



Design and characterization of specMACS

F. Ewald et al.

Title Page

Abstract

Introduction

Conclusions

References

Tables

Figures

⏪

⏩

◀

▶

Back

Close

Full Screen / Esc

Printer-friendly Version

Interactive Discussion



To recover from a reduced integration time, the auto exposure control periodically tries to increase the integration time t_{int} . To this end, the histograms of the last 150 frames are periodically extrapolated to the next longer integration time $t_{\text{int}}(i + 1)$. If the extrapolated histograms do not trigger the overexposure protection described above, $t_{\text{int}}(i)$ is increased to $t_{\text{int}}(i + 1)$. Thereby any increase of integration time is tested before it is actually performed and suppressed if the signal limit set by the quantile limit would be exceeded.

3.2.2 Automatic dark frame

Another task of the control software is the automation of dark signal measurements. During dark signal measurements, it is obviously not possible to perform real measurements, so the amount of time spent with dark signal measurements is to be minimized. However, the dark signal varies with time, so the automation is set up to measure approximately 30 dark frames at least every two minutes. Since the dark signal additionally changes with integration time $t_{\text{int}}(i)$, the system checks if a recent dark signal measurement with the current sensor settings was obtained and if not, triggers a dark signal measurement before changing $t_{\text{int}}(i)$.

3.2.3 Scriptable measurements

In order to control and repeat complex measurement tasks, the CAMPAign ASsistant (CAMPAS) was developed. It is a domain specific scripting language combined with a communication library which has access to all system components. Using CAMPAS the user can define measurement tasks like a hemispherical scan through step-by-step instructions. These instructions control the behavior of the sensors, the scanning mount and all other system components combined. The CAMPAS system furthermore provides simple access to various dynamic coordinates (e.g. sun position or the current position of other instruments). Thus a general task can be written once and repeated many times, which increases comparability of results.

4 Characterization and calibration methods

There are three essential characteristics which define the overall performance of imaging spectrometers. First, the radiometric response of the instrument has to be known to obtain absolute radiometric measurements. Secondly, a precise knowledge about the spectral projection onto the sensor is required to put the radiometric values into context. Concluding, information about the spatial projection and its geometric distortions are required to assess the spatial image quality and its resolution. Armed with this information measured raw data can be converted into physical units during the calibration procedure. Additional to the measured raw data, several auxiliary datasets are needed for the calibration procedure. This auxiliary data includes dark current measurements made before and after each measurement as well as the instrument characteristics obtained during a laboratory characterization.

A guideline through the whole process and the involved quantities is given by the calibration flow chart in Fig. 7. The process follows Lenhard et al. (2015) closely and is extended by a nonlinearity correction regarding integration time explained in Sect. 4.1.3. The following subsections will cover each of the displayed steps.

In the following all variables are given as pixel-wise properties when not mentioned otherwise. Temporal averaged properties of the sensor will be identified with angle brackets while spatial averages will be indicated with an overbar. The laboratory characterization of the specMACS sensors was performed at the Calibration Home Base (CHB) (Gege et al., 2009) of the Remote Sensing Technology Institute (IMF) of the German Aerospace Center (DLR).

4.1 Radiometric characterization

The sensors consist of many mostly independent pixels of which each acts as a radiance sensor for its specific spectral and spatial section of the full image. Each pixel outputs the measured signal as a digital number. To obtain an absolute radiometric value the sensor has to be calibrated since its signal is subject to influences other than

AMTD

8, 9853–9925, 2015

Design and characterization of specMACS

F. Ewald et al.

Title Page

Abstract

Introduction

Conclusions

References

Tables

Figures



Back

Close

Full Screen / Esc

Printer-friendly Version

Interactive Discussion



the impinging light. The sensor signal S can be modeled as a sum of a radiometric signal S_0 containing only radiance information, S_d which describes the dark signal of the sensor and the noise \mathcal{N} of the sensor:

$$S = S_0 + S_d + \mathcal{N} \quad (2)$$

5 In the following subsections noise \mathcal{N} , dark signal S_d and radiometric signal S_0 will be independently examined. In the remaining subsections bad pixels and optical performance like angular and spectral bandwidth as well as keystone effects will be discussed.

4.1.1 Noise

10 The noise \mathcal{N} is composed of dark current noise \mathcal{N}_{dc} , read noise \mathcal{N}_{read} and photon shot noise \mathcal{N}_{shot} . Their joint standard deviation $\sigma_{\mathcal{N}}$ is calculated using the individual standard deviations σ_{shot} , σ_{dc} and σ_{read} :

$$\sigma_{\mathcal{N}} = \sqrt{\sigma_{shot}^2 + \sigma_{dc}^2 + \sigma_{read}^2} = \sqrt{k^2 N + \sigma_{dark}^2} \quad (3)$$

15 Since photons arrive randomly in time the number N of photoelectrons measured during a fixed time interval is distributed according to the Poisson distribution. Following the Poisson statistics the standard deviation $\sigma_{\mathcal{N}}$ of a distribution with the expectation value N is proportional to \sqrt{N} . For this reason the photon shot variance σ_{shot}^2 scales linearly with the number of incoming photoelectrons N and the squared conversion gain k^2 [DN²] (Eq. 3). For a sensor with linear response, the relation $S_0 \propto N$ holds. A deviation from this relationship can be an indication for a nonlinear relationship between the number N of photoelectrons and the photoelectric signal S_0 or is caused by a non-Poisson noise source.

20 Similar to the dark signal S_d in S , a dark noise \mathcal{N}_{dark} remains in \mathcal{N} without illumination. It is comprised of dark current noise \mathcal{N}_{dc} and readout noise \mathcal{N}_{read} . The dark

Design and characterization of specMACS

F. Ewald et al.

Title Page

Abstract

Introduction

Conclusions

References

Tables

Figures



Back

Close

Full Screen / Esc

Printer-friendly Version

Interactive Discussion



current noise is caused by statistical variation of thermally generated electrons. Like the photon noise its origin is a random process and therefore exhibits a Poisson distribution. Pixel readout and analog to digital conversion is further subject to electronic readout noise, which is independent from integration time.

5 With the classic Photon Transfer Curve (PTC) (Janesick, 2007) the noise characteristics can be used to determine many important camera parameters. When the signal noise standard deviation $\sigma_{\mathcal{N}}$ is plotted against the mean, darkcurrent-corrected signal level $\langle S_0 \rangle$ on a log-log scale different noise regimes become apparent. The dark noise at integration time $t_{\text{int}} = 0$ s at the lower end of $\langle S_0 \rangle$ is dominated by read-out noise with standard deviation σ_{read} . With increasing mean signal level $\langle S_0 \rangle$ photon shot noise becomes dominant with σ_{shot} . Due to the Poisson-like distribution the photon shot noise variance σ_{shot}^2 should scale linearly with mean signal level. Deviations from this linear relationship can provide an indication of a nonlinear radiometric response (Bohndiek et al., 2008) or a charge sharing mechanism between pixels (Downing et al., 2006; Stefanov, 2014).

10 Since both sensors can not be homogeneously illuminated (as required in classic PTC) due to the spectrographic diffraction grating, the noise standard deviation $\sigma_{\mathcal{N}}$ and mean, darkcurrent-corrected signal level $\langle S_0 \rangle$ are calculated individually for each pixel. For this analysis $\sigma_{\mathcal{N}}$ is calculated as the pixel-wise standard deviation of 500 consecutive frames measured on an integrating sphere for multiple integration times t_{int} . As noise \mathcal{N} describes unbiased temporal variations of the signal around its expectation value, its temporal mean vanishes: $\langle \mathcal{N} \rangle \approx 0$.

15 In addition to noise, pixel sensors are also subject to inter-pixel variations caused by imperfections in the sensor material and electronics. These variations are almost constant in time but become evident on uncorrected images as visible noise pattern. This pattern is generally called fixed pattern noise (FPN) and can be mitigated through calibration using characterized parameters from the following sections. Long term variations of the FPN can be covered through periodic recharacterization of the sensor.

**Design and
characterization of
specMACS**

F. Ewald et al.

Title Page

Abstract

Introduction

Conclusions

References

Tables

Figures



Back

Close

Full Screen / Esc

Printer-friendly Version

Interactive Discussion



4.1.2 Dark signal

Inherent to all electronic imaging sensors is the dark signal S_d . It is a pixel dependent offset and its variation between pixels is often described as dark signal non-uniformity. The total signal S is composed of the photoelectric signal S_0 , a dark signal S_d and the remaining noise \mathcal{N} (Eq. 2). When the shutter is closed and subsequently the photoelectric signal $S_0 = 0$, an averaged $\langle S_d \rangle$ can directly be measured as $\langle \mathcal{N} \rangle \rightarrow 0$:

$$\langle S \rangle = \langle S_0 + S_d + \mathcal{N} \rangle = \langle S_d \rangle + \langle \mathcal{N} \rangle \approx \langle S_d \rangle \quad (4)$$

The dark signal S_d is further composed of the dark current signal $S_{dc} = s_{dc}t_{int}$ and the readout offset S_{read} :

$$S_d = s_{dc}t_{int} + S_{read} \quad (5)$$

s_{dc} is also known as reverse leakage current and is a characteristic of all diodes. It originates from thermally generated electrons and holes within the semiconductor material. Since the electrons are randomly generated over time the dark current signal S_{dc} increases linearly with s_{dc} and integration time t_{int} . The remaining offset S_{read} is caused by the readout process and is therefore independent from t_{int} .

The dark signal analysis was done under controlled laboratory conditions during calibration within the CHB facility as well as on one flight during the ACRIDICON-CHUVA campaign. In order to suppress the noise during lab analysis, 500 consecutive dark frames were averaged. Dark frames were measured for 9 different integration times while ambient air temperatures were held constant by air-conditioning. During the measurements the temperature in the VNIR casing remained stable at 312.0K. Since the SWIR camera is not equipped with a temperature sensor the VNIR temperature has been used as a proxy.

For the analysis during the flight only 30 consecutive dark frames were averaged to minimize gaps between radiometric measurements. Analysis of mean dark signal levels $\overline{S_d}$ inflight over all pixels was done for both spectrometers using integration times

Design and characterization of specMACS

F. Ewald et al.

Title Page

Abstract

Introduction

Conclusions

References

Tables

Figures



Back

Close

Full Screen / Esc

Printer-friendly Version

Interactive Discussion



which leads to the form in Eq. (8). Furthermore we found a small mismatch between the integration time set t_{set} and the actual integration time t_{int} . For this reason an offset term t_{ofs} was added to be fitted in the model in Eq. (8).

The model which describes the observed photoelectric signal S_0 then reads:

$$S_0 = s_n(t_{\text{set}} + t_{\text{ofs}}) + \gamma(s_n(t_{\text{set}} + t_{\text{ofs}}))^2 \quad (8)$$

Here, γ is the nonlinearity of S_0 in DN^{-1} and t_{ofs} is the offset between actual and reported integration time. The model can be inverted to yield the normalized signal s_n from measured signal S , dark signal S_d and t_{set} when γ and t_{ofs} are known:

$$s_n = \frac{\sqrt{4\gamma(S - S_d) + 1} - 1}{2\gamma(t_{\text{set}} + t_{\text{ofs}})} \xrightarrow{\gamma \rightarrow 0} \frac{S - S_d}{t_{\text{set}} + t_{\text{ofs}}} \quad (9)$$

This nonlinear model converges to the linear model in Eq. (7) for $\gamma \rightarrow 0$ and $t_{\text{ofs}} \rightarrow 0$.

4.1.4 Absolute radiometric response

After nonlinearity correction the normalized signal s_n in $[\text{DNms}^{-1}]$ can be converted into absolute radiance values L in $[\text{mWm}^{-2}\text{nm}^{-1}\text{sr}^{-1}]$. Using the absolute radiometric response R in $[\text{DNms}^{-1}\text{mW}^{-1}\text{m}^2\text{nm sr}]$, this can be described by

$$L = R^{-1} \cdot s_n. \quad (10)$$

R is different for each pixel and thereby also covers the correction of inter-pixel variations of the sensor response, also called photo response non-uniformity (PRNU). The absolute radiometric response R is determined once during a radiometric calibration with a known radiance standard.

In this work the absolute radiometric response R was characterized using the absolute RAdiance STAndard (RASTA) (Schwarzmaier et al., 2012) of the IMF at DLR-EOC which was characterized with absolute radiance standards operated by the PTB (Physical. Techn. Bundesanstalt), the German National Metrology Institute. As the RASTA

Design and characterization of specMACS

F. Ewald et al.

Title Page

Abstract

Introduction

Conclusions

References

Tables

Figures



Back

Close

Full Screen / Esc

Printer-friendly Version

Interactive Discussion



polarization insensitive signal offset. When the measurements with the rotating polarizer are fitted to the model in Eq. (12) the polarization sensitivity P can be determined as the ratio between the polarization sensitive signal amplitude A and the polarization insensitive signal offset O :

$$P = \frac{A}{O} \cdot 100\% \quad (13)$$

The maximum signal loss due to the polarization sensitivity then occurs at the angular offset ϕ_0 with respect to the entrance slit.

4.2 Spatial and spectral characterization

Besides the radiometric characterization of the spectrometer its spatial and spectral projection onto the detector are of great importance for the scientific application. The radiance contribution for a single pixel from different solid angles is described by two line spread functions (LSF), the across- and along-track LSFs. The spectral responsivity for every pixel is described by a spectral response function (SRF). Moreover some of the pixels of the detector yield unreliable (dead pixel) or biased (hot pixel) measurements, which should be marked and classified as “bad”.

4.2.1 Bad pixel characterization

Bad pixels are pixels which do not behave according to the instrument model assumed by the calibration procedure. As already argued by Lenhard et al. (2015), bad pixel characterization of an assembled hyperspectral sensor is not straight forward as a uniform illumination of the sensor chip is not achievable due to the dispersing element. It was decided to manually observe measured data and keep track of pixels which do obviously behave very different from surrounding pixels in a list associated with the calibration files. For the VNIR sensor, there existed no previous knowledge about bad pixels. For the SWIR sensor, the manufacturer provided list of bad pixels was included.

Design and characterization of specMACS

F. Ewald et al.

Title Page

Abstract

Introduction

Conclusions

References

Tables

Figures



Back

Close

Full Screen / Esc

Printer-friendly Version

Interactive Discussion



Currently one bad pixel is known for the VNIR sensor and 264 bad pixels are known for the SWIR sensor.

4.2.2 Bad pixel correction

Bad pixel correction or the replacement of invalid pixel values by interpolated values is needed if further processing algorithms can not handle invalid pixels in the resulting dataset. Depending on the goal of the proceeding analysis, different interpolation schemes may be appropriate. Currently, bad pixel correction is implemented based on the list of bad pixels provided by the calibration file and a user defined strategy how interpolation rules should be derived from the bad pixel list. The primarily used strategy is to perform a linear interpolation from spatially adjacent good pixels over a single or a group of bad pixels in order to keep spectral features intact.

4.2.3 Response function

Due to asymmetric distortions of the LSFs of both sensors and the SRFs of the SWIR sensor a fit with a Gaussian function G would yield distorted estimates of center and resolution. For this reason a third order B-spline fit F is used to retrieve the center and the resolution respectively bandwidth of the response functions. The center of a response function is determined by the median x_c of F .

The resolution Δx is centered around x_c and determined by the area under the normalized spline fit F , which is equal to the area under a Gaussian function $G(x)$ between its full width half maximum FWHM. This way a measure of the response function width is provided in analogy to the full width half-maximum (FWHM) of a Gaussian shaped function. Consequently the resolution Δx can be derived using:

$$\frac{\int_{x_c - \Delta x/2}^{x_c + \Delta x/2} F(x) dx}{\int_{-\infty}^{\infty} F(x) dx} = \frac{\int_{-FWHM/2}^{FWHM/2} G(x) dx}{\int_{-\infty}^{\infty} G(x) dx} = 0.7610 \quad (14)$$

Design and characterization of specMACS

F. Ewald et al.

Title Page

Abstract

Introduction

Conclusions

References

Tables

Figures



Back

Close

Full Screen / Esc

Printer-friendly Version

Interactive Discussion



This is also illustrated in Fig. 8a. Using this technique the angular resolution $\Delta\theta$ and the spectral bandwidth $\Delta\lambda$ are determined.

4.2.4 Spatial characterization

The information about the geometric properties of the spectrometers is contained in the across- and along-track LSFs, namely the viewing angles θ_c and the angular resolution $\Delta\theta$. As already defined in the beginning along-track means perpendicular to the instrument spatial slit while across-track means parallel to the spatial slit. Every pixel of the sensor arrays has its set of individual LSFs. The viewing angles θ_c of one spatial pixel along the spectral axis are ideally the same. Any deviation is commonly called keystone, which is expressed as the maximum difference of the viewing angles of one spatial pixel. The width of LSFs $\Delta\theta$ across- and along-track determines the sharpness of the spatial image.

The geometric and spectral characterizations were done analogous to Gege et al. (2009) and Baumgartner et al. (2012). The measurement setup consists of a narrow slit with a width of 0.05 mm, illuminated by a Quartz Tungsten Halogen lamp and positioned at the focal plane of a reflective collimator with a focal length of 750 mm. This results in a collimated beam with a divergence of 0.07 mrad that is guided via a folding mirror onto the aperture of the spectrometer. Through linear movement and simultaneous rotation of the folding mirror, different spatial pixels can be illuminated. The collimated beam is large enough to fill the aperture of the spectrometer.

The across-track LSFs are measured by using a slit which is imaged perpendicular to the entrance slit of the spectrograph. The angular scan for the selected pixels is accomplished by changing the illumination angle via the folding mirror over a range of 0.7 rad. For the VNIR this scan is done in increments of 0.14 mrad covering the entire FOV. In case of the SWIR instrument, the scan is performed in increments of 0.35 mrad.

The along-track LSFs are measured at 7 angles that are evenly distributed over the FOVs of the instruments. They are measured by using a slit that is imaged parallel to the entrance slit of the spectrograph. The incidence angle of the collimated beam on

Design and characterization of specMACS

F. Ewald et al.

Title Page

Abstract

Introduction

Conclusions

References

Tables

Figures



Back

Close

Full Screen / Esc

Printer-friendly Version

Interactive Discussion



Design and characterization of specMACS

F. Ewald et al.

Title Page

Abstract

Introduction

Conclusions

References

Tables

Figures



Back

Close

Full Screen / Esc

Printer-friendly Version

Interactive Discussion



the spectrometer aperture is changed by a along-track translation of the illuminated slit in the focal plane of the collimator. For the measurement of the selected spatial pixels of the VNIR, the along-track LSF is scanned over a range of 6.06 mrad in increments of 0.3 mrad, and for the SWIR over a range of 5.9 mrad in increments of 0.15 mrad.

To retrieve the viewing angles and angular resolutions from the measurements, the measured data was interpolated using splines as described in Sect. 4.2.3. The geometric along track values of pixels that are not measured directly are inferred by interpolation of the viewing angles and angular resolution in between the measured spatial pixels. For the interpolation a second order polynomial fit to the measured spatial pixel is used. The order of the polynomial functions is selected so that higher order polynomials do not reduce the residuals significantly more. The keystone distortion of one spatial line is defined as the largest difference of across-track viewing angles along the spectral axis.

4.2.5 Spectral characterization

To determine the spectral properties of the imaging spectrometers, the spectral response functions (SRF) of the spectral channels need to be characterized. For one spectral channel the SRF center and its width can vary over the FOV of the instrument, i.e. every single pixel of the sensor array has its individual SRF, similar to the LSFs. The deviation of the center wavelength λ_c within a spatial line is commonly described as spectral smile while the SRF width gives the spectral bandwidth $\Delta\lambda$. In the following the spectral smile will be given as the deviation of λ_c with respect to the center pixel within each spatial line.

To measure the SRF, a collimated beam of nearly monochromatic light from a monochromator is used. The collimated beam is guided into the spectrometer's aperture by the already mentioned folding mirror that allows for the illumination of a selectable spatial pixel. To guarantee that the spectrometer aperture and IFOV are completely illuminated, the beam cross-section is larger than the aperture and the beam divergence is larger than the IFOV of the spectrometer. The monochromator has an ab-

Design and characterization of specMACS

F. Ewald et al.

Title Page

Abstract

Introduction

Conclusions

References

Tables

Figures



Back

Close

Full Screen / Esc

Printer-friendly Version

Interactive Discussion



solute uncertainty of ± 0.1 nm for wavelengths below 1000 nm, and ± 0.2 nm for longer wavelengths. The spectral bandwidth is set to 0.65 nm for the measurement of the VNIR and 1.3 nm for the measurement of the SWIR. Computations indicate that the chosen bandwidth of the monochromator has only very little influence on the measured bandwidths as long as the monochromator bandwidth is smaller than the measured bandwidth and its SRF is known. With a Gaussian monochromator SRF well below the specified spectrometer bandwidth both requirements are met. For the measurement of the SRFs of the VNIR, the wavelength of the monochromator is scanned from 400 to 1030 nm in steps of 1 nm, and for the SWIR, from 940 to 2550 nm in steps of 2 nm. Due to time constraints, these measurements are only feasible for a small subset of all spatial pixels: For both sensors, the SRFs are measured at seven angles evenly distributed over their across-track FOV.

To determine the two relevant parameters of the SRF, the center wavelength λ_c and the bandwidth $\Delta\lambda$, a Gaussian function is fitted to the data measured for each spectral channel of the VNIR. The center wavelength is then given by the center position of the Gaussian, and the bandwidth as the full width at half maximum (FWHM). For the SWIR a spline is fitted to the data (see Sect. 4.2.3) as the SRFs can not be represented accurately with a Gaussian function as it can be seen in Fig. 8b.

The spectral properties of the other pixels are inferred by fitting the center wavelengths and bandwidths with a second order polynomial. This procedure assumes that the properties of the optical system do not vary rapidly on the scale of the detector array. This assumption holds for the specMACS imaging spectrometers, which was validated using spectral line lamps. The spectral smile for each spatial pixel is computed as the difference between its wavelength and the wavelength of the center pixel within the same spectral channel.

The measurement setup is described in more detail in Gege et al. (2009) and details about the data analysis as well as a validation of the approach for another hyperspectral camera can be found in Baumgartner et al. (2012).

4.2.6 Optical distortion correction

Optical distortion correction can be performed through interpolation of the dataset onto a regular grid. As the adequate grid is problem dependent and interpolation for every pixel is costly in terms of computing power and lossy in terms of information content, this interpolation step should be performed during spatial rectification of the image. Hereby the optical characterization for each instrument is combined with the location data for each frame, which is then stored together with the radiometric signal from each pixel. Subsequently this meta data can be used in the transformation onto the final target coordinate system.

5 Characterization results

5.1 Radiometric properties

5.1.1 Noise

Figure 9 shows the results of the noise analysis which was obtained from the nonlinearity measurements with varying integration times as listed in Table 2. For each pixel and each integration time, the mean and standard deviation was calculated and accumulated in the shown 2-D histograms. The noise characteristics of the VNIR are shown on the left while results for the SWIR are shown on the right. On top in Fig. 9 the pixel-wise standard deviation $\sigma_{\mathcal{N}}$ is plotted against the mean, darkcurrent-corrected signal level $\langle S_0 \rangle$ on a log-log scale. On the bottom, the same is done with the pixel-wise variance $\sigma_{\mathcal{N}}^2$ on a linear scale.

At low values of $\langle S_0 \rangle$ the signal-independent read-out noise becomes apparent. The read-out noise for $t_{\text{int}} = 0$ s is derived as the y -intercept of a constant fit on $\sigma_{\mathcal{N}}$ for $\langle S_0 \rangle < 30$ DN. By doing this, the noise associated with the readout channel was found

Title Page

Abstract

Introduction

Conclusions

References

Tables

Figures



Back

Close

Full Screen / Esc

Printer-friendly Version

Interactive Discussion



to be 5.0DN for the VNIR and 4.5DN for the SWIR spectrometer. For larger values of $\langle S_0 \rangle$ the noise begins to increase.

When the standard deviation $\sigma_{\mathcal{N}}$ is fitted with the square root model following Eq. (3) the noise characteristics can be further investigated. At first glance, the noise standard deviation of the VNIR sensor is in accordance with the noise model described by Eq. (3) with a constant conversion gain $k = 0.043$ [DN]. For values of S_0 between 0–2000 DN it follows the function

$$\sigma_{\mathcal{N}} = \sqrt{0.043S_0 + 5.07^2} \text{ [DN]}. \quad (15)$$

For larger values the noise variance $\sigma_{\mathcal{N}}^2$ no longer scales linearly with $\langle S_0 \rangle$ but remains below the fit in Eq. (15). As seen in Fig. (9) bottom left, the VNIR noise can no longer be explained by a Poisson noise model (Eq. 3) with a constant conversion gain k [DN]. This noise characteristic can be an indication for two different mechanisms at work. Either k [DN] varies with signal level S_0 , which would cause a photon response non-linearity (PRNL) or a charge sharing is occurring between pixels which would violate the Poisson assumption. A more in-depth analysis of the noise showed a small auto-correlation within pixels of the same spatial sensor row, which would suggest the latter. But as the PRNL analysis in Sect. 5.1.3 will show, radiometric nonlinearity has to be considered as well as a possible explanation.

In contrast the SWIR noise standard deviation $\sigma_{\mathcal{N}}$ shown in Fig. 9, top right compares much better to the Poisson model. Between 0–12 000 DN it fits the following form:

$$\sigma_{\mathcal{N}} = \sqrt{0.015S_0 + 4.77^2} \text{ [DN]} \quad (16)$$

At larger values of $\langle S_0 \rangle$ the noise variance $\sigma_{\mathcal{N}}^2$ remains linear with $k = 0.015$ [DN] until saturation is reached. For both sensors no wavelength dependence in noise was found.

Design and characterization of specMACS

F. Ewald et al.

Title Page

Abstract

Introduction

Conclusions

References

Tables

Figures



Back

Close

Full Screen / Esc

Printer-friendly Version

Interactive Discussion



5.1.2 Dark signal

The analysis of the dark signal shows clear differences between the sensors used for the VNIR and the SWIR spectrometer. Figure 10 (right) shows mean dark signal levels $\overline{S_d}$ in available digital number range when averaging over 30 dark frames as measured during a flight of the aircraft campaign ACRIDICON-CHUVA. The green curve shows the readings from a temperature sensor located within the casing of the VNIR spectrometer. While the level of $\overline{S_d}$ for the SWIR depends on integration time t_{int} as well as on temperature, the level of $\overline{S_d}$ for the VNIR seems independent from t_{int} and temperature. The typical variation of the dark signal within a minute was around 10DN for the SWIR and 3DN for the VNIR.

A more in-depth analysis of this behavior is shown in Fig. 10 (left) where measurements of S_d in a controlled lab environment (CHB) are compared with measurements of $\overline{S_d}$ during the mentioned flight. The slope of the regression line reflects the dependence of $\overline{S_d}$ on t_{int} while the shaded area shows the influence of temperature on this relationship. In Fig. 10 (left) the non-uniformity of S_d is shown by error bars, which is only significant in the case of the SWIR. With temperature increasing from 310.4 to 320.0K the number of thermally generated electrons per second increases from 352 DN ms⁻¹ to 494.0 DN ms⁻¹ for the SWIR sensor. In this temperature range the VNIR sensor shows only a marginal influence on dark signal levels. In contrast, a considerable amount of dynamic range is lost to the dark signal in the case of the SWIR.

In the case of the VNIR there is mainly a fixed dark signal offset independent of t_{int} . Since thermally generated electrons do not play an important role in dark signal generation within the VNIR sensor the independence of S_d from t_{int} and temperature is evident. In order to push the dark signal below the photoelectric signal the HgCdTe-based detector of the SWIR spectrometer has to be cooled down to 200K. Although the SWIR sensor is equipped with a thermoelectric cooler the dark signal S_d in Fig. 10 is obviously still influenced by air temperature fluctuations.

Design and characterization of specMACS

F. Ewald et al.

Title Page

Abstract

Introduction

Conclusions

References

Tables

Figures



Back

Close

Full Screen / Esc

Printer-friendly Version

Interactive Discussion



Design and characterization of specMACS

F. Ewald et al.

Title Page

Abstract

Introduction

Conclusions

References

Tables

Figures



Back

Close

Full Screen / Esc

Printer-friendly Version

Interactive Discussion



Additionally dark signal offsets S_{read} exhibit a slight dependence on temperature in both spectrometers. The offsets S_{read} between both sensors differ fundamentally with respect to their pixel-wise distribution and the fixed pattern noise they are creating. While FPN^{VNIR} appears smooth with $\sigma_{\text{FPN}}^{\text{VNIR}} = 9.4 \text{ DN}$ the spatial distribution of FPN^{SWIR} is very uneven with $\sigma_{\text{FPN}}^{\text{SWIR}} = 173.8 \text{ DN}$. Figure 11 shows FPN^{SWIR} . Bad pixels that were excluded in this analysis are also shown. Without correction of this offset by subtraction of a promptly measured dark frame the spectral as well as the spatial SWIR measurements would be strongly biased.

5.1.3 Nonlinear radiometric response

Using the integration times in Table 2 and the model described in Sect. 4.1.3, the parameters γ and t_{ofs} were determined for every pixel. This was done for measurements taken on the large integrating sphere at the CHB facility on 3 July 2014 by regression of measured S_0 on Eq. (8) using the least squares method. Since solar radiances are naturally very strong signals the model in Eq. (8) was not designed to model effects at very low signal levels. For this reason the fit was only done for pixels with signal levels higher than 2 % of the maximum signal level. Mean and standard deviation of γ and t_{ofs} over the sensor are shown in Table 3. The fact that γ and t_{ofs} do not vary much across pixels allows the general applicability of this values to all pixels for simplicity.

For the VNIR camera the nonlinearity causes a deviation of 9 % from the linear model at maximum signal level while the SWIR camera does not exhibit a noticeable nonlinearity. In contrast t_{ofs} of the VNIR camera is negligible with 0.001 ms while the SWIR offset 0.055 ms lies within the same order of magnitude as the shortest possible integration time of 0.1 ms.

5.1.4 Absolute Radiometric Response

As described in Sect. 4.1.4 the calibration was transferred from the absolute radiance standard RASTA to the large integrating sphere for both specMACS cameras and a

Design and characterization of specMACS

F. Ewald et al.

Title Page

Abstract

Introduction

Conclusions

References

Tables

Figures



Back

Close

Full Screen / Esc

Printer-friendly Version

Interactive Discussion



third spectrometer (SVC-HR1024i) independently from each other. The absolute radiometric response R of the VNIR and the SWIR camera are presented in Fig. 12. Both sensors show strongly reduced sensitivity at the upper and lower boundaries of the spectrum, which is expected due to the nature of the material dependent band-gap and the transmissivity of the optical system. The VNIR sensor shows an etalon fringe pattern (seen in Fig. 12(left) along the spectral dimension) typical for backside-illuminated sensors (Marques Vatus and Magnan, 2004), whereas the front-illuminated SWIR sensor does not exhibit significant patterns. The discrepancy between the found absolute radiometric responses R and the ones given by the manufacturer does not exceed more than 10 %.

In Fig. 13a the spectral radiance of the large integrating sphere is shown as it was transferred from the RASTA standard using Eq. (11). With the LIS illuminating the complete FOV of the instrument the conversion from normalized signals to absolute radiances (Eq. 10) is calculated for each pixel. This conversion is described by the absolute radiometric response R . Using the nominal accuracies of the reference light sources and signal statistics derived from the sensors during characterization measurements, an error budget for the absolute radiometric response R was calculated and is shown as 2σ uncertainty in Fig. 13b. The uncertainty in the absolute radiometric calibration of the RASTA was given by the PTB and is indicated by the green line in Fig. 13b. At longer wavelengths the nominal uncertainty of the RASTA increases, which can be traced back to the accuracy of the reference radiometers used during the RASTA characterization at the PTB. The uncertainty due to inhomogeneities of the LIS is given to be $\pm 1.6\%$ (Baumgartner, 2013). Another source of uncertainty arises from the drift of the dark signal S_d over time and from the noise \mathcal{N} of the signal S , which is shown as blue (VNIR) and red (SWIR) dashed lines. The drift per minute was assumed to be 10DN in case of the SWIR and 3DN in case of the VNIR as found in the dark signal analysis (Sect. 4.1.2). The noise was calculated for 100 averaged dark frames and 500 averaged illuminated frames resulting in $\sigma_{(S)} = 0.5$ DN. At the RASTA and the LIS the 2σ uncertainty due to the dark signal drift and noise accounts to around 1 % in case of

Design and characterization of specMACS

F. Ewald et al.

Title Page

Abstract

Introduction

Conclusions

References

Tables

Figures



Back

Close

Full Screen / Esc

Printer-friendly Version

Interactive Discussion



the VNIR and 3% in case of the SWIR for wavelengths in the center of both spectra. While the dark signal drift and noise level stays constant with wavelength the radiometric sensitivity and therefore the signal S decreases towards the edges of the spectra. This results in a sharp increase of the relative uncertainty towards spectral regions with low radiometric sensitivity. In particular towards the edges of the spectra, the drift of the dark signal S_d contributes the most to the overall radiometric uncertainty. Altogether this error budget is a very conservative estimate for an individual measurement with a single pixel without any averaging. For relative measurements some of these uncertainties cancel out e.g. the LIS inhomogeneity and the RASTA uncertainty during a window transmissivity characterization presented in Sect. 6.2.

5.1.5 Polarization sensitivity

The results of the polarization sensitivity measurement are shown in Fig. 14. The polarization sensitivity P and the angular offset ϕ_0 were found by fitting measurements of light with different polarization angles to Eq. (12). For the VNIR on the left and for the SWIR on the right, Fig. 14 shows the polarization sensitivity P for all pixels. With the entrance slit oriented horizontally in Fig. 14 the angular offset ϕ_0 is indicated by the black solid lines. For this polarization orientation the polarization dependent signal loss becomes maximal for the particular pixel. For real measurements, when the polarization degree and orientation is unknown, the maximum radiometric error is given by $P/2$. The polarization sensitivity P can be observed to increase from 2 to 10% towards larger wavelengths for both cameras. While P is higher in the center of the VNIR FOV, it increases towards the edges in case of the SWIR. Furthermore very high values for P (>10%) can be observed at both wavelength cutoffs of the SWIR, where the radiometric sensitivity becomes very small. Due to the very low radiometric sensitivity of the SWIR the region of shortest wavelengths were excluded in this analysis. The values of P agree well with Lenhard et al. (2015) and Hyvarinen et al. (1998) and can be explained by the polarization caused at the entrance slit and the holographic transmission grating.

5.2 Spatial and spectral properties

5.2.1 Spatial characteristics

A typical LSF for the VNIR sensor is shown in Fig. 8a. As already mentioned in Sect. 4.2.3 the LSFs can not be accurately approximated with Gaussian functions. Therefore splines were fitted to the data to compute the viewing angles θ_c and the angular resolution $\Delta\theta$ of both spectrometers related to the usual FWHM values for a Gaussian shaped sensitivity. The characterization results for both sensors are shown in Fig. 15 and in Tables 4 and 5. Due to low sensitivity some channels of the sensors could not be evaluated accurately. Therefore, the first 30 channels of the VNIR and the first 17 channels of the SWIR sensor are not taken into account. Figure 15a and c show the deviations of the across track viewing angles θ_c relative to spectral channel 400 for the VNIR and to spectral channel 128 for the SWIR sensor. Ripples in Fig. 15a and b are caused by the etalon effect in the VNIR. For both spectrometers the strongest keystone distortion occurs at longer wavelengths while its mean value of 0.30 mrad in the VNIR and 0.50 mrad in the SWIR remain well below the angular resolution of the sensors.

Figure 15b and d show the across track angular resolution $\Delta\theta$ of the sensors. The area with the smallest $\Delta\theta$ and therefore sharpest pixel is stretched across the sensor FOV. At longer wavelengths and lower pixel numbers the VNIR image projection gets rather blurry. Besides the achromatism this behaviour could be explained by a slightly misaligned entrance slit with respect to the entrance optics. Considering the mean ratio of 3.15 between angular resolution and sampling and the fact that only parts of the image appear sharp the VNIR shows a reduced focusability. The sharpest SWIR image projection is approximately at the center in wavelength but asymmetric in lower pixel numbers as it can be seen in Fig. 15d. With a mean angular oversampling of 1.95 the SWIR optics produce a sharper image on the detector. However the angular sampling (1.94 mrad) and resolution (3.79 mrad) is far coarser than in the case of the VNIR (0.44 and 1.37 mrad).

Design and characterization of specMACS

F. Ewald et al.

Title Page

Abstract

Introduction

Conclusions

References

Tables

Figures



Back

Close

Full Screen / Esc

Printer-friendly Version

Interactive Discussion



6 Airborne deployment during ACRIDICON

One of the first deployments of the full specMACS setup characterised in the previous sections was the aircraft campaign ACRIDICON CHUVA in Amazon region around Manaus, Brazil in September 2014 (Wendisch et al., 2015). specMACS was installed on the German research aircraft HALO (High Altitude LONG range aircraft, Krautstrunk and Giez, 2012) for cloud side observations. Additional characteristics specific to this aircraft setup and first results are presented in the next section.

6.1 Setup on board HALO

In cooperation with enviscope GmbH specMACS was mounted into a HALO Rack looking sideways with vertical spatial axis. For this task a specifically designed window for the HALO side view port had to be developed to ensure a high transmissivity over the whole spectral range of specMACS (Fig. 17). Into two vertical apertures inside the side view port two 2 cm thick purified quartz glass panes (Herasil 102, Haereus) were embedded. To address the problem of window icing, a fan was installed below the window, which constantly blows warm cabin air onto the inner window surface.

The cameras' field of view was tilted 5° downward with respect to the horizontal axis of the airplane. After matching both cameras field of views, a combined usable field of view of 21° below to 11° above the lateral axis is available.

During the airborne operation the across-track pixel size for clouds in a distance of 5 km is around 2.2 m in case of the VNIR and 9.7 m in case of the SWIR in accordance with their respective angular sampling. In order to obtain a comparable spatial along-track resolution the frame rate is set to 30 fps. With a maximum ground speed of 800 km h^{-1} the pixel size for clouds in this distance becomes $2.2 \times 7.4 \text{ m}$ in case of the VNIR and $9.7 \times 7.4 \text{ m}$ in case of the SWIR. Internal storage was designed large enough to enable continuous measurements for at least 2 flights of 8 h duration.

Since the instrument was fixed in one of the measurement racks of HALO, the captured data has to be rectified during post processing to correct for the airplane move-

AMTD

8, 9853–9925, 2015

Design and characterization of specMACS

F. Ewald et al.

Title Page

Abstract

Introduction

Conclusions

References

Tables

Figures



Back

Close

Full Screen / Esc

Printer-friendly Version

Interactive Discussion



Design and characterization of specMACS

F. Ewald et al.

Title Page

Abstract

Introduction

Conclusions

References

Tables

Figures

◀

▶

◀

▶

Back

Close

Full Screen / Esc

Printer-friendly Version

Interactive Discussion



ments. The spatial rectification can be done using inertial navigation systems (INS) provided by the BASic HALO Measurement And Sensor System (BAHAMAS) (Krautstrunk and Giez, 2012) or by the Spectral Modular Airborne Radiation measurement sysTem (SMART) (Wendisch et al., 2001) whose subsystems offer both a 100 Hz data stream of accurate position information. All specMACS measurements were time referenced using the central time server provided by BAHAMAS.

For ACRIDICON, the modular software system was set up to allow fully automated measurements (Sect. 3.2). An additional user interface is shown on the integrated monitor, which allows the flight scientists to have an immediate overview of the most relevant system parameters and gives the possibility to manually override the automated system.

6.2 Window transmission

The transmission of the quartz glass windows were characterized radiometrically and spectrally on the CHB Large Integrating Sphere by comparing specMACS measurements of the sphere with and without the windows in the optical path. The angular dependence of the window transmission was further characterized at three different angles between the optical axis of the sensors and the window (0° = perpendicular to the optical axis, 11.8° = angle as mounted on HALO, 15.5° = steepest angle possible with the chosen experimental setup). Note that the transmission

$$T = \frac{L_{Win}}{L} = \frac{R^{-1} S_{n;Win}}{R^{-1} S_n} = \frac{S_{n;Win}}{S_n} \quad (17)$$

can be calculated based on the darkcurrent and nonlinearity corrected signals alone and without using the characterization of the absolute radiometric response. In addition to the laboratory characterization, theoretical reflection losses of the window surface including internal reflections were calculated using refractive indices from the glass data sheet and Snell's and Fresnel's laws for comparison.

using spectral radiance data from the VNIR camera. Calibrated radiances at 2200 and 2100nm are shown below in Fig. 20b and c. Since the ice absorption is stronger at 2100nm compared to 2200nm the cloud ice phase becomes visible as evident drop in radiance at 2200 nm.

7 Conclusions and outlook

The hardware design and the modular and resilient software design enables the specMACS system to be used as a versatile data acquisition system for hyperspectral measurements in the wavelength range of 417 to 2496nm. The design can easily be adapted to ground and airborne measurements and can be extended to or combined with even more sensors (like a long wave infrared camera) naturally. The reliable software concept allowed to measure throughout the whole ACRIDICON 2014 campaign autonomously and without any measurement interruptions.

The laboratory characterization of the VNIR and SWIR sensors revealed important details of the behaviour of the sensors needed for a scientific application of specMACS. Especially the characterization of the previously unknown nonlinear behavior of the VNIR enables a consistent calibration of data measured with both sensors simultaneously and thereby allows for a sound comparison between signals of both sensors. The available error budget calculations allow to estimate to which extent measured effects are actually significant.

Concluding the most important results of this study the following points must be considered during the measurement with specMACS and during the subsequent calibration of its scientific data.

1. For both instruments no serious internal straylight and ghost images have been found. When direct sunlight impinges on the front optics stray light baffles become indispensable.

Design and characterization of specMACS

F. Ewald et al.

Title Page

Abstract

Introduction

Conclusions

References

Tables

Figures



Back

Close

Full Screen / Esc

Printer-friendly Version

Interactive Discussion



Design and characterization of specMACS

F. Ewald et al.

Title Page

Abstract

Introduction

Conclusions

References

Tables

Figures



Back

Close

Full Screen / Esc

Printer-friendly Version

Interactive Discussion



2. Due to the variable dark current level of the SWIR sensor prompt and frequent dark signal measurements for every used integration time and sensor temperature are essential to achieve the specified radiometric accuracy. Interpolation of dark signal frames from before and after each measurement are needed to compensate for the SWIR dark current drift of ± 10 DN per minute. In contrast, the VNIR dark signal shows no strong dependence on integration time or sensor temperature since it is mainly caused by readout noise.
3. The radiometric response R given from the manufacturer does not differ by more than 10 % from R found in this work. Since this deviation is in the range of the radiometric calibration uncertainty, R seems to be quite stable over time.
4. In case of the SWIR we have found a small mismatch between the integration time set t_{set} and the actual integration time t_{int} . For this reason we introduced an additional term t_{ofs} to compensate for this mismatch.
5. The radiometric response of the VNIR shows a nonlinear behaviour at medium to large signal levels, which leads to an underestimation of the absolute radiometric signal if not corrected.
6. During the spatial characterization the VNIR sharpness turned out to be suboptimal. Besides a slight achromatism the focus seems to shift in the across-track direction with wavelength.
7. The spectral bandwidth is within specifications for both spectrometers. The spectral sampling is sufficient for both instruments while the oversampling of the VNIR spectrometer allows the reduction of the spectral sampling by half without losing information significantly.
8. During the spectral and spatial characterization no significant spectral smile or keystone was found for both cameras.

**Design and
characterization of
specMACS**

F. Ewald et al.

Title Page

Abstract

Introduction

Conclusions

References

Tables

Figures



Back

Close

Full Screen / Esc

Printer-friendly Version

Interactive Discussion



9. Both sensors exhibit a certain polarization sensitivity, which for the most part remains well below 10 %. For completely polarized light with unknown polarization orientation an additional radiometric error of 5 % has to be taken into account.

The final evaluation shows that the instrument performance complies with the accuracy requirements stated in the introduction. Absolute radiometric accuracy well below the mentioned 3-D radiative effects can be achieved when the described signal calibration procedure is applied. This is also confirmed by the good agreement between both spectrometers in the overlap region around 1000 nm. Spectral calibration accuracy fully meets the requirements of current microphysical cloud retrievals and enables reliable identification of gaseous absorption lines. Below 1000 nm the spectral bandwidth should be sufficient for the analysis of absorption line depths of features like the oxygen A-band.

As shown exemplarily in Sect. 6, data acquired during the ACRIDICON 2014 campaign offers many possibilities for data analysis. The in-situ data simultaneously acquired by other participating institutions yields a unique opportunity to validate retrieved remote sensing results with directly measured cloud properties. As mentioned before the focus of data analysis for this campaign will be on cloud side remote sensing. That means, cloud microphysical parameters, like glaciation height or liquid water droplet size, will be evaluated for the visible vertical profile.

Acknowledgements. We thank Meinhard Seefeldner and Anton Lex for their great support in constructing and building the stray light protection and many other mechanical parts for the specMACS system. F. Ewald gratefully acknowledges funding of parts of this work by the German Research Foundation (DFG) under grant number MA 2548/9-1. We thank Karim Lenhard and Peter Gege (IMF) for their support during the laboratory characterization. We would also like to thank enviscope GmbH (D. Schell), Uni Leipzig (M. Wendisch), Max Planck Institute for Chemistry (U. Pöschl) and DLR Institute of Atmospheric Physics (M. Rapp) for their support in adapting and operating specMACS on HALO.

References

- Aikio, M.: Hyperspectral prism-grating-prism imaging spectrograph, Technical Research Centre of Finland Heinola, Finland, 36–78, 2001. 9858
- Armstrong, J.: Programming Erlang, The Pragmatic Bookshelf, Raleigh, NC and Dallas, TX, USA, 1–383, 2007. 9864
- Baumgartner, A.: Characterization of Integrating Sphere Homogeneity with an Uncalibrated Imaging Spectrometer, in: Proc. WHISPERS 2013, 1–4, 2013. 9883
- Baumgartner, A., Gege, P., Köhler, C., Lenhard, K., and Schwarzmaier, T.: Characterisation methods for the hyperspectral sensor HySpex at DLR's calibration home base, in: Sensors, Systems, and Next-Generation Satellites XVI, vol. 85331H, doi:10.1117/12.974664, 2012. 9876, 9878
- Bohndiek, S. E., Blue, A., Clark, A., Prydderch, M., Turchetta, R., Royle, G., and Speller, R.: Comparison of Methods for Estimating the Conversion Gain of CMOS Active Pixel Sensors, IEEE Sensors Journal, 8, 1734–1744, doi:10.1109/JSEN.2008.2004296, 2008. 9869
- Bragg, W. H. and Bragg, W. L.: The Reflection of X-rays by Crystals, Proceedings of the Royal Society of London A: Mathematical, Physical and Engineering Sciences, 88, 428–438, doi:10.1098/rspa.1913.0040, 1913. 9860
- Bréon, F. and Doutriaux-Boucher, M.: A comparison of cloud droplet radii measured from space, Geoscience and Remote Sensing, IEEE Transactions on, 43, 1796–1805, 2005. 9857
- Chiu, J. C., Marshak, A., Huang, C.-H., Várnai, T., Hogan, R. J., Giles, D. M., Holben, B. N., O'Connor, E. J., Knyazikhin, Y., and Wiscombe, W. J.: Cloud droplet size and liquid water path retrievals from zenith radiance measurements: examples from the Atmospheric Radiation Measurement Program and the Aerosol Robotic Network, Atmos. Chem. Phys., 12, 10313–10329, doi:10.5194/acp-12-10313-2012, 2012. 9855
- Coddington, O. M., Pilewskie, P., Redemann, J., Platnick, S., Russell, P. B., Schmidt, K. S., Gore, W. J., Livingston, J., Wind, G., and Vukicevic, T.: Examining the impact of overlying aerosols on the retrieval of cloud optical properties from passive remote sensing, J. Geophys. Res., 115, D10211, doi:10.1029/2009JD012829, 2010. 9855
- Cornet, C., Buriez, J.-C., Riédi, J., Isaka, H., and Guillemet, B.: Case study of inhomogeneous cloud parameter retrieval from MODIS data, Geophys. Res. Lett., 32, L13807, doi:10.1029/2005GL022791, 2005. 9857

Design and characterization of specMACS

F. Ewald et al.

Title Page

Abstract

Introduction

Conclusions

References

Tables

Figures



Back

Close

Full Screen / Esc

Printer-friendly Version

Interactive Discussion



Design and characterization of specMACS

F. Ewald et al.

Title Page

Abstract

Introduction

Conclusions

References

Tables

Figures



Back

Close

Full Screen / Esc

Printer-friendly Version

Interactive Discussion



Downing, M., Baade, D., Sinclair, P., Deiries, S., and Christen, F.: CCD riddle: a) signal vs time: linear; b) signal vs variance: non-linear, in: High Energy, Optical, and Infrared Detectors for Astronomy II, vol. 6276, p. 627609, doi:10.1117/12.671457, 2006. 9869

Dury, M. R., Theocharous, T., Harrison, N., Fox, N., and Hilton, M.: Common black coatings – reflectance and ageing characteristics in the 0.32 – 14.3 μ m wavelength range, Opt. Commun., 270, 262–272, doi:10.1016/j.optcom.2006.08.038, 2007. 9862

Dworak, A., Charrue, P., Ehm, F., Sliwinski, W., and Sobczak, M.: Middleware Trends And Market Leaders 2011, Proceedings of ICALEPCS2011, CERN-ATS-2011-196, 1334–1337, <http://accelconf.web.cern.ch/AccelConf/icalleps2011/papers/frbhmult05.pdf> (last access: 15 July 2015), 2011. 9864

Dworak, A., Ehm, F., Charrue, P., and Sliwinski, W.: The new CERN Controls Middleware, J. Phys. Conf. Ser., 396, 012017, doi:10.1088/1742-6596/396/1/012017, 2012. 9864

Ehrlich, A., Bierwirth, E., Wendisch, M., Gayet, J.-F., Mioche, G., Lampert, A., and Heintzenberg, J.: Cloud phase identification of Arctic boundary-layer clouds from airborne spectral reflection measurements: test of three approaches, Atmos. Chem. Phys., 8, 7493–7505, doi:10.5194/acp-8-7493-2008, 2008. 9855, 9889

Ehrlich, A., Wendisch, M., Bierwirth, E., Gayet, J.-F., Mioche, G., Lampert, A., and Mayer, B.: Evidence of ice crystals at cloud top of Arctic boundary-layer mixed-phase clouds derived from airborne remote sensing, Atmos. Chem. Phys., 9, 9401–9416, doi:10.5194/acp-9-9401-2009, 2009. 9855

Eichler, H., Ehrlich, A., Wendisch, M., Mioche, G., Gayet, J.-F., Wirth, M., Emde, C., and Minikin, A.: Influence of ice crystal shape on retrieval of cirrus optical thickness and effective radius: A case study, J. Geophys. Res.-Atmos., 114, D19203, doi:10.1029/2009JD012215, 2009. 9855

Ewald, F., Zinner, T., and Mayer, B.: Remote sensing of particle size profiles from cloud sides: Observables and retrievals in a 3D environment, in: AIP Conference Proceedings, vol. 1531, 83–86, AIP Publishing, 2013. 9856

Fischer, J. and Grassl, H.: Detection of Cloud-Top Height from Backscattered Radiances within the Oxygen A Band. Part 1: Theoretical Study, J. Appl. Meteorol., 30, 1245–1259, 1991. 9858

Fossum, E.: CMOS image sensors: electronic camera-on-a-chip, IEEE Transactions on Electron Devices, 44, 1689–1698, doi:10.1109/16.628824, 1997. 9860

Design and characterization of specMACS

F. Ewald et al.

Title Page

Abstract

Introduction

Conclusions

References

Tables

Figures



Back

Close

Full Screen / Esc

Printer-friendly Version

Interactive Discussion



Gege, P., Fries, J., Haschberger, P., Schötz, P., Schwarzer, H., Strobl, P., Suhr, B., Ulbrich, G., and Vreeling, W. J.: Calibration facility for airborne imaging spectrometers, *ISPRS Journal of Photogrammetry and Remote Sensing*, 64, 387–397, doi:10.1016/j.isprsjprs.2009.01.006, 2009. 9867, 9876, 9878

Hansen, J. and Pollack, J.: Near-infrared light scattering by terrestrial clouds, *J. Atmos. Sci.*, 27, 265–281, 1970. 9855

Hewitt, C., Bishop, P., and Steiger, R.: A Universal Modular ACTOR Formalism for Artificial Intelligence, in: *Proceedings of the 3rd International Joint Conference on Artificial Intelligence, IJCAI'73*, 235–245, Morgan Kaufmann Publishers Inc., San Francisco, CA, USA, available at: <http://dl.acm.org/citation.cfm?id=1624775.1624804> (last access: 15 July 2015), 1973. 9864

Hintjens, P.: ZeroMQ: The Guide, available at: <http://zguide.zeromq.org/page:all> (last access: 15 July 2015), 2010. 9864

Holben, B., Eck, T., Slutsker, I., Tanre, D., Buis, J., Setzer, A., Vermote, E., Reagan, J., Kaufman, Y., Nakajima, T. Y., Lavenu, F., Jankowiak, I., and Smirnov, A.: AERONET - a federated instrument network and data archive for aerosol characterization, *Remote Sens. Environ.*, 66, 1–16, 1998. 9855

Houghton, J., Ding, Y., Griggs, D., Noguer, M., van der Linden, P., Dai, X., Maskell, K., and Johnson, C.: *Climate change 2001: The scientific basis*, Tech. rep., 427–431, 2001. 9856

Hyvarinen, T. S., Herrala, E., and Dall'Ava, A.: Direct sight imaging spectrograph: a unique add-on component brings spectral imaging to industrial applications, in: *Digital Solid State Cameras: Designs and Applications*, 3302, 165–175, doi:10.1117/12.304581, 1998. 9884

Jäkel, E., Walter, J., and Wendisch, M.: Thermodynamic phase retrieval of convective clouds: impact of sensor viewing geometry and vertical distribution of cloud properties, *Atmos. Meas. Tech.*, 6, 539–547, doi:10.5194/amt-6-539-2013, 2013. 9855

Janesick, J. R.: *Photon Transfer*, SPIE Publications, Bellingham, WA, USA, p. 49, 2007. 9869, 9871

Jørgensen, R. N.: *The VTTVIS line imaging spectrometer: principles, error sources, and calibration*, Risø National Laboratory, 11–68, 2002. 9858

Kikuchi, N., Nakajima, T., Kumagai, H., Kuroiwa, H., Kamei, A., Nakamura, R., and Nakajima, T. Y.: Cloud optical thickness and effective particle radius derived from transmitted solar radiation measurements: Comparison with cloud radar observations, *J. Geophys. Res.-Atmos.*, 111, D07205, doi:10.1029/2005JD006363, 2006. 9855

Design and characterization of specMACS

F. Ewald et al.

Title Page

Abstract

Introduction

Conclusions

References

Tables

Figures



Back

Close

Full Screen / Esc

Printer-friendly Version

Interactive Discussion



- Krautstrunk, M. and Giez, A.: The Transition From FALCON to HALO Era Airborne Atmospheric Research, in: Atmospheric Physics, edited by: Schumann, U., Research Topics in Aerospace, 609–624, Springer Berlin Heidelberg, http://link.springer.com/chapter/10.1007/978-3-642-30183-4_37 (last access: 15 July 2015), 2012. 9887, 9888
- 5 LeBlanc, S. E., Pilewskie, P., Schmidt, K. S., and Coddington, O.: A spectral method for discriminating thermodynamic phase and retrieving cloud optical thickness and effective radius using transmitted solar radiance spectra, *Atmos. Meas. Tech.*, 8, 1361–1383, doi:10.5194/amt-8-1361-2015, 2015. 9855
- 10 Lenhard, K., Baumgartner, A., and Schwarzmaier, T.: Independent Laboratory Characterization of NEO HySpex Imaging Spectrometers VNIR-1600 and SWIR-320m-e, *Geoscience and Remote Sensing, IEEE Transactions on*, 53, 1828–1841, doi:10.1109/TGRS.2014.2349737, 2015. 9858, 9867, 9873, 9874, 9884
- 15 Marques Vatus, C. and Magnan, P.: Analysis and potentialities of backside-illuminated thinned CMOS imagers, in: *Detectors and Associated Signal Processing*, 5251, 178–186, doi:10.1117/12.513893, 2004. 9883
- Marshak, A., Martins, J. V., Zubko, V., and Kaufman, Y. J.: What does reflection from cloud sides tell us about vertical distribution of cloud droplet sizes?, *Atmos. Chem. Phys.*, 6, 5295–5305, doi:10.5194/acp-6-5295-2006, 2006a. 9856
- 20 Marshak, A., Platnick, S., Varnai, T., Wen, G., and Cahalan, R. F.: Impact of three-dimensional radiative effects on satellite retrievals of cloud droplet sizes, *J. Geophys. Res.*, 111, D09207, 2006b. 9857
- Martins, J. V., Marshak, A., Remer, L. A., Rosenfeld, D., Kaufman, Y. J., Fernandez-Borda, R., Koren, I., Correia, A. L., Zubko, V., and Artaxo, P.: Remote sensing the vertical profile of cloud droplet effective radius, thermodynamic phase, and temperature, *Atmos. Chem. Phys.*, 11, 9485–9501, doi:10.5194/acp-11-9485-2011, 2011. 9856, 9857, 9889
- 25 McBride, P. J., Schmidt, K. S., Pilewskie, P., Kittelman, A. S., and Wolfe, D. E.: A spectral method for retrieving cloud optical thickness and effective radius from surface-based transmittance measurements, *Atmos. Chem. Phys.*, 11, 7235–7252, doi:10.5194/acp-11-7235-2011, 2011. 9855
- 30 Nakajima, T. Y. and King, M. D.: Determination of the optical thickness and effective particle radius of clouds from reflected solar radiation measurements. Part I: Theory, *J. Atmos. Sci.*, 47, 1878–1893, 1990. 9855, 9857

Design and characterization of specMACS

F. Ewald et al.

Title Page

Abstract

Introduction

Conclusions

References

Tables

Figures



Back

Close

Full Screen / Esc

Printer-friendly Version

Interactive Discussion



- Pilewskie, P., Pommier, J., Bergstrom, R., Gore, W., Rabbette, M., Schmid, B., Hobbs, P. V., and Tsay, S. C.: Solar spectral radiative forcing during the Southern African regional science initiative, *J. Geophys. Res.-Atmos.*, 108, 8486, doi:10.1029/2002JD002411, 2003. 9855
- Rosenfeld, D., Williams, E., Andreae, M. O., Freud, E., Pöschl, U., and Rennó, N. O.: The scientific basis for a satellite mission to retrieve CCN concentrations and their impacts on convective clouds, *Atmos. Meas. Tech.*, 5, 2039–2055, doi:10.5194/amt-5-2039-2012, 2012. 9856
- Schmidt, K., Pilewskie, P., Platnick, S., Wind, G., Yang, P., and Wendisch, M.: Comparing irradiance fields derived from Moderate Resolution Imaging Spectroradiometer airborne simulator cirrus cloud retrievals with solar spectral flux radiometer measurements, *J. Geophys. Res.*, 112, D24206, doi:10.1029/2007JD008711, 2007. 9855
- Schwarzmaier, T., Baumgartner, A., Gege, P., Köhler, C., and Lenhard, K.: DLR's New Traceable Radiance Standard "RASTA", in: *International Geoscience and Remote sensing Symposium (IEEE, 2012)*, 1–4, available at: <http://elib.dlr.de/78116/> (last access: 15 July 2015), 2012. 9872
- Stefanov, K.: A Statistical Model for Signal-Dependent Charge Sharing in Image Sensors, *IEEE T. Electron Dev.*, 61, 110–115, doi:10.1109/TED.2013.2291448, 2014. 9869
- Twomey, S. and Cocks, T.: Remote sensing of cloud parameters from spectral reflectance in the near-infrared, *Beiträge zur Physik der Atmosphäre*, 62, 172–179, 1989. 9855
- Varnai, T. and Marshak, A.: Observations of three-dimensional radiative effects that influence satellite retrievals of cloud properties, *Quarterly Journal of the Hungarian Meteorological Society*, 106, 265–278, 2002. 9857
- Wendisch, M. and Mayer, B.: Vertical distribution of spectral solar irradiance in the cloudless sky – A case study, *Geophys. Res. Lett.*, 30, doi:10.1029/2002GL016529, 2003. 9855
- Wendisch, M., Müller, D., Schell, D., and Heintzenberg, J.: An airborne spectral albedometer with active horizontal stabilization, *J. Atmos. Ocean. Tech.*, 18, 1856–1866, 2001. 9855, 9888
- Wendisch, M., Pöschl, U., Andreae, M. O., Machado, L. A. L., Albrecht, R., Schlager, H., Rosenfeld, D., Martin, S. T., Abdelmonem, A., Afchine, A., Araujo, A., Artaxo, P., Aufmhoff, H., Barbosa, H. M. J., Borrmann, S., Braga, R., Buchholz, B., Cecchini, M. A., Costa, A., Curtius, J., Dollner, M., Dorf, M., Dreiling, V., Ebert, V., Ehrlich, A., Ewald, F., Fisch, G., Fix, A., Frank, F., Fütterer, D., Heckl, C., Heidelberg, F., Hueneke, T., Jaekel, E., Jaervinen, E., Jurkat, T., Kanter, S., Kästner, U., Kenntner, M., Kesselmeier, J., Klimach, T., Knecht, M., Kohl, R., Kölling,

Design and characterization of specMACS

F. Ewald et al.

Title Page

Abstract

Introduction

Conclusions

References

Tables

Figures



Back

Close

Full Screen / Esc

Printer-friendly Version

Interactive Discussion



T., Kraemer, M., Krüger, M., Krisna, T. C., Lavric, J. V., Longo, K., Mahnke, C., Manzi, A. O., Mayer, B., Mertes, S., Minikin, A., Molleker, S., Münch, S., Nillius, B., Pfeilsticker, K., Pöhlker, C., Roiger, A., Rose, D., Rosenow, D., Sauer, D., Schnaiter, M., Schneider, J., Schulz, C., de Souza, R. A. F., Spanu, A., Stock, P., Vila, D., Voigt, C., Walser, A., Walter, D., Weigel, R., Weinzierl, B., Werner, F., Yamasoe, M. A., Ziereis, H., Zinner, T., and Zöger, M.: The ACRIDICON-CHUVA campaign to study tropical deep convective clouds and precipitation using the new German research aircraft HALO, B. Am. Meteorol. Soc., submitted, 2015. 9887

Zinner, T. and Mayer, B.: Remote sensing of stratocumulus clouds: Uncertainties and biases due to inhomogeneity, J. Geophys. Res., 111, D14209, doi:10.1029/2005JD006955, 2006. 9857

Zinner, T., Marshak, A., Lang, S., Martins, J. V., and Mayer, B.: Remote sensing of cloud sides of deep convection: towards a three-dimensional retrieval of cloud particle size profiles, Atmos. Chem. Phys., 8, 4741–4757, doi:10.5194/acp-8-4741-2008, 2008. 9856, 9857



Figure 1. specMACS VNIR and SWIR sensors on scanning mount. The stray light protection is prominently visible in front of the sensors.

Design and characterization of specMACS

F. Ewald et al.

Title Page

Abstract

Introduction

Conclusions

References

Tables

Figures

◀

▶

◀

▶

Back

Close

Full Screen / Esc

Printer-friendly Version

Interactive Discussion



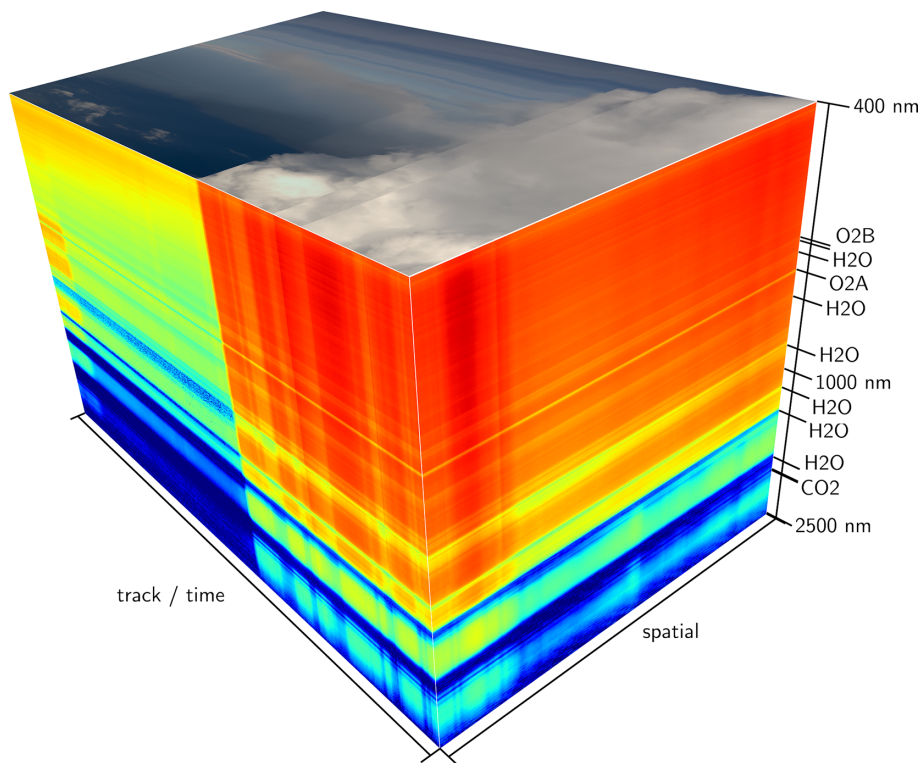


Figure 2. An exemplary hyperspectral data cube as measured with specMACS. It illustrates the data available from measurements with the instrument. On the top surface, an RGB image is shown as it would be seen by a human observer. Underlying this image the spectrum from 400–2500 nm available for every pixel is indicated. Clearly visible are absorption bands of O₂, H₂O and CO₂.

**Design and
characterization of
specMACS**

F. Ewald et al.

Title Page

Abstract

Introduction

Conclusions

References

Tables

Figures

◀

▶

◀

▶

Back

Close

Full Screen / Esc

Printer-friendly Version

Interactive Discussion



Design and characterization of specMACS

F. Ewald et al.

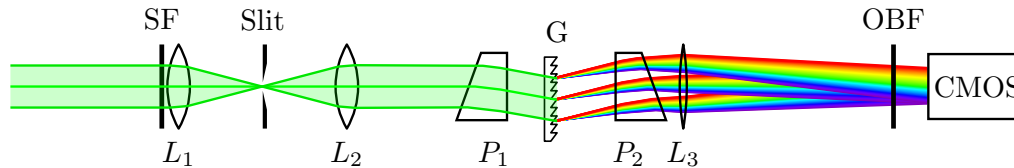


Figure 3. Optical concept of hyperspectral imagers. Sketch of the light path entering the instrument as it first gets spatially filtered by a slit and subsequently separated by a holographic grating: SF ~ Spectral Flattening Filter, L_1 ~ Front optics, L_2 ~ Collimator, P_1 ~ Entry Prism, G ~ Volume Phase Holographic Transmission Grating, P_2 ~ Exit Prism, L_3 ~ Focuser, OBF ~ Order Blocking Filter, CMOS ~ Imaging Sensor.

Title Page

Abstract

Introduction

Conclusions

References

Tables

Figures

◀

▶

◀

▶

Back

Close

Full Screen / Esc

Printer-friendly Version

Interactive Discussion



AMTD

8, 9853–9925, 2015

Design and characterization of specMACS

F. Ewald et al.

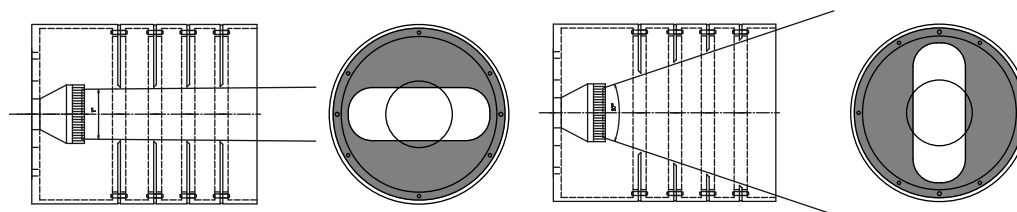


Figure 4. Design of stray light protection. Left: cut along spectral axis, right: cut along the spatial axis.

Title Page

Abstract

Introduction

Conclusions

References

Tables

Figures



Back

Close

Full Screen / Esc

Printer-friendly Version

Interactive Discussion



**Design and
characterization of
specMACS**

F. Ewald et al.

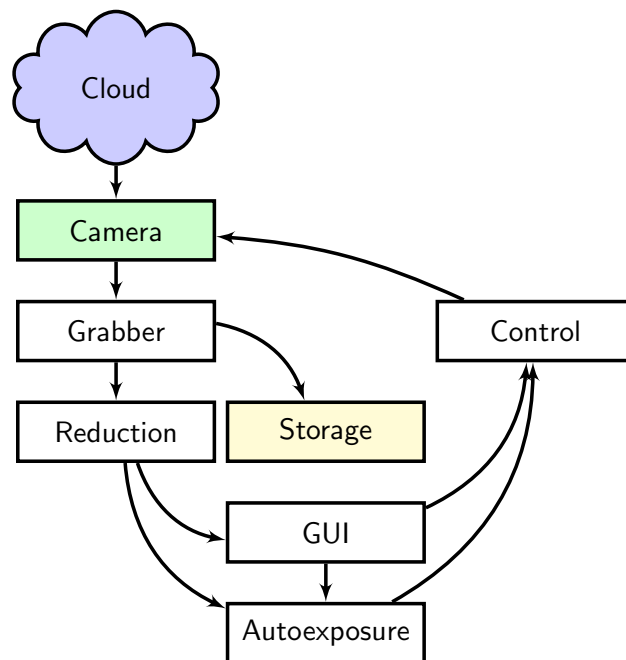


Figure 5. Simplified overview of the data flow: image data gets stored early and reduced extracts are sent simultaneously to the Graphical User Interface and automated control systems to adapt the acquisition settings of the sensor hardware.

[Title Page](#)[Abstract](#)[Introduction](#)[Conclusions](#)[References](#)[Tables](#)[Figures](#)[◀](#)[▶](#)[◀](#)[▶](#)[Back](#)[Close](#)[Full Screen / Esc](#)[Printer-friendly Version](#)[Interactive Discussion](#)

Design and characterization of specMACS

F. Ewald et al.

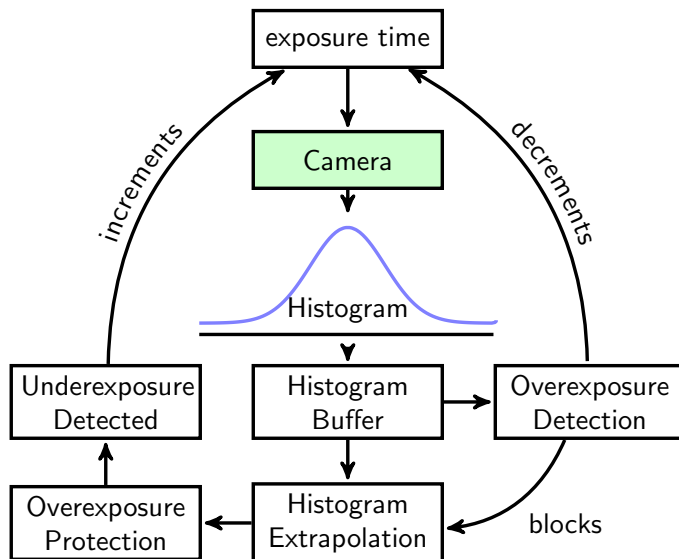


Figure 6. Overview of the automated exposure control system.

Title Page

Abstract

Introduction

Conclusions

References

Tables

Figures

⏪

⏩

◀

▶

Back

Close

Full Screen / Esc

Printer-friendly Version

Interactive Discussion



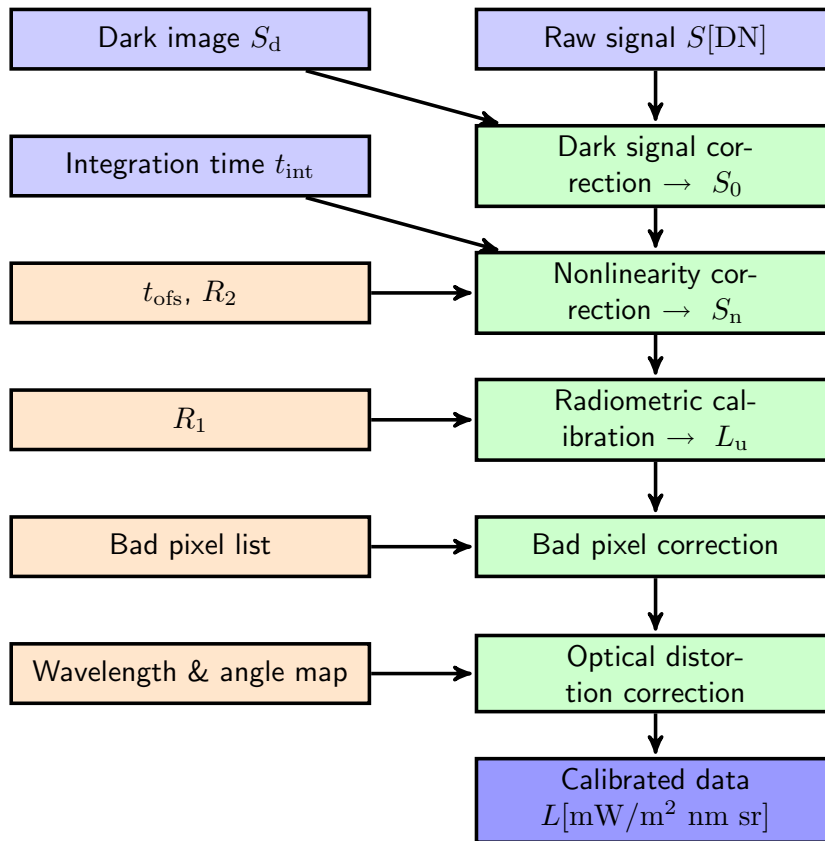


Figure 7. Schematic calibration with nonlinearity correction] Schematic calibration using the newly developed nonlinearity correction. Light blue boxes are measured data, orange boxes are characterization data, green boxes are calibration steps and dark blue is the calibrated data.

**Design and
characterization of
specMACS**

F. Ewald et al.

Title Page	
Abstract	Introduction
Conclusions	References
Tables	Figures
◀	▶
◀	▶
Back	Close
Full Screen / Esc	
Printer-friendly Version	
Interactive Discussion	



Design and characterization of specMACS

F. Ewald et al.

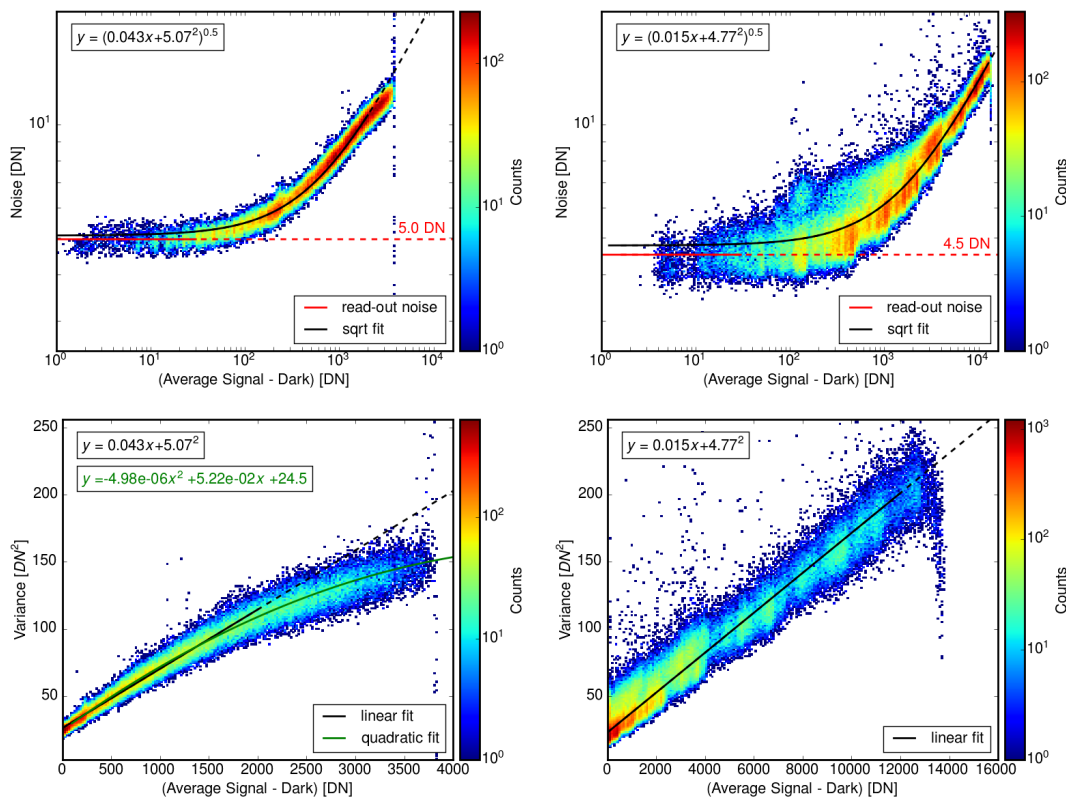


Figure 9. Noise characteristics for the (left) VNIR and (right) SWIR spectrometer. (top) The noise σ_N (standard deviation of S) is shown against the mean, darkcurrent-corrected signal level $\langle S_0 \rangle$. (bottom) Noise variance σ_N^2 against $\langle S_0 \rangle$ for both spectrometers.

Title Page

Abstract

Introduction

Conclusions

References

Tables

Figures

◀

▶

◀

▶

Back

Close

Full Screen / Esc

Printer-friendly Version

Interactive Discussion



Design and characterization of specMACS

F. Ewald et al.

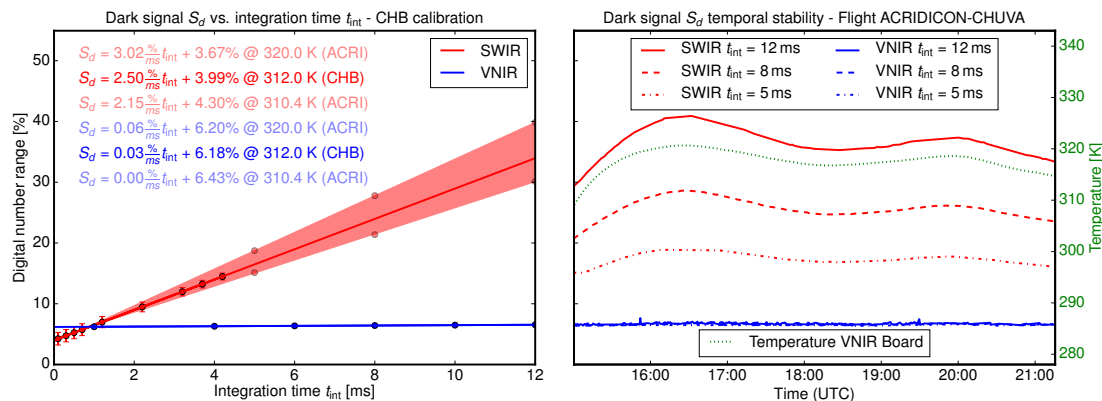


Figure 10. (left) Mean dark signal levels $\overline{S_d}$ in DN as a function of integration time t_{int} when averaging over 500 dark frames as observed during the CHB calibration. (right) $\overline{S_d}$ when averaging over 30 dark frames as observed on one flight AC14 (21 September 2014) during the ACRIDICON-CHUVA campaign. The blue lines show $\overline{S_d}$ for the VNIR, red lines for the SWIR spectrometer while the different linestyles denote different integration times. The green curve shows the temperature as measured within the VNIR casing. In both plots the dependence of $\overline{S_d}$ from temperature and integration time becomes clearly visible for the SWIR, while $\overline{S_d}$ remains constant for the VNIR.

[Title Page](#)
[Abstract](#)
[Introduction](#)
[Conclusions](#)
[References](#)
[Tables](#)
[Figures](#)
[◀](#)
[▶](#)
[◀](#)
[▶](#)
[Back](#)
[Close](#)
[Full Screen / Esc](#)
[Printer-friendly Version](#)
[Interactive Discussion](#)


Design and characterization of specMACS

F. Ewald et al.

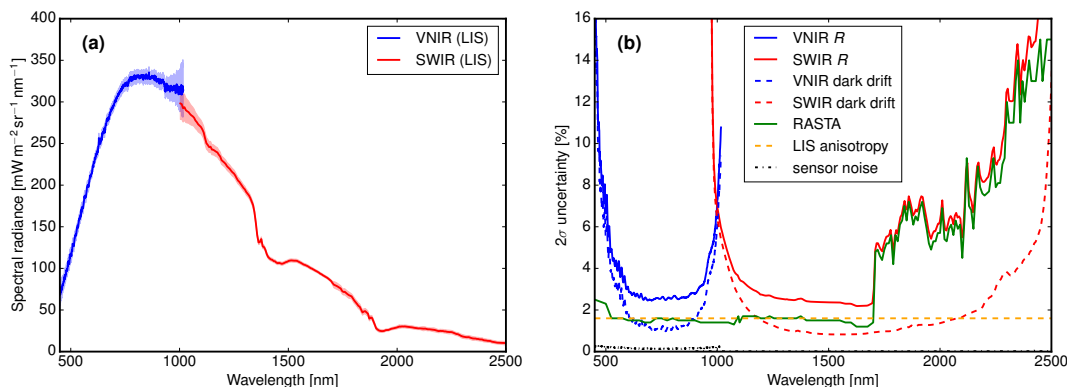


Figure 13. (a) Reconstructed spectral radiance on top the large integrating sphere during the respective radiometric characterization. The absolute radiometric values were transferred from the RASTA base standard using the specMACS VNIR and SWIR sensors. The 2σ -uncertainty associated with the radiometric calibration is shown by the filled area. (b) Main contributions to the 2σ -uncertainty of the absolute radiometric response R . The uncertainties resulting from sensor noise and dark current drift are exemplary shown for the RASTA measurements. Due to the lower radiance of the RASTA, other noise and drift components contribute less to the total error.

[Title Page](#)
[Abstract](#)
[Introduction](#)
[Conclusions](#)
[References](#)
[Tables](#)
[Figures](#)
[◀](#)
[▶](#)
[◀](#)
[▶](#)
[Back](#)
[Close](#)
[Full Screen / Esc](#)
[Printer-friendly Version](#)
[Interactive Discussion](#)

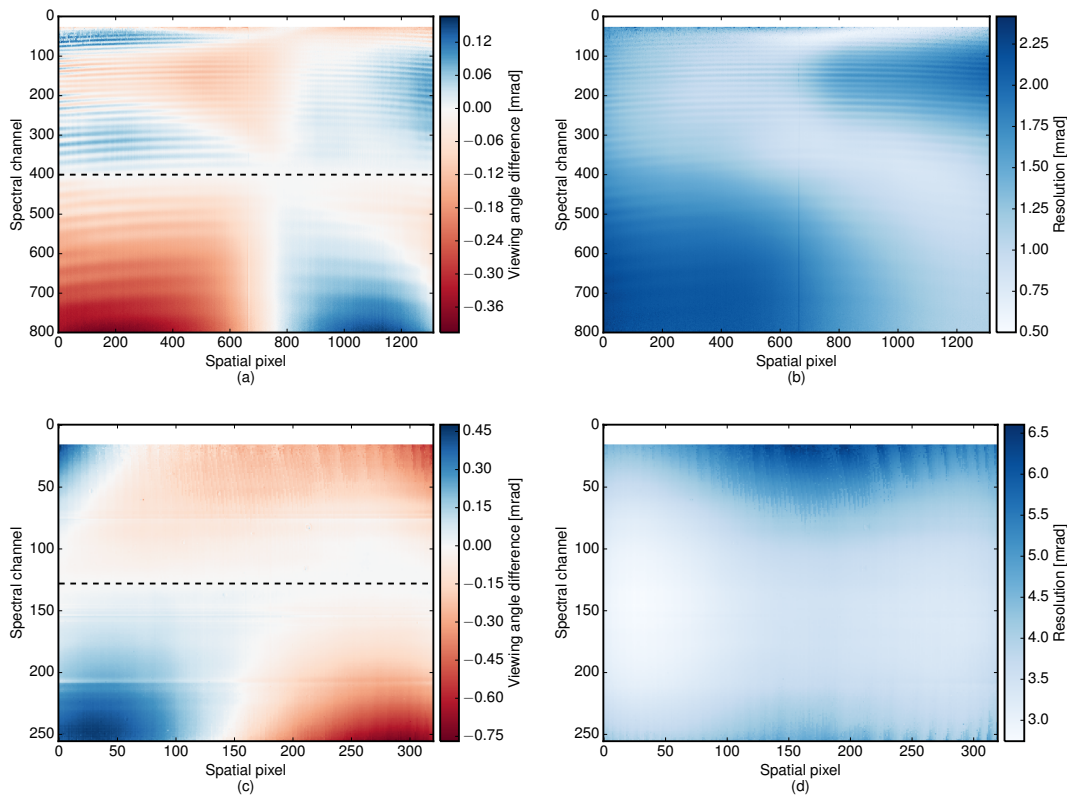



Figure 15. Spatial across track characterization results of the VNIR (top) and SWIR (bottom) sensor. **(a)** and **(c)** show the difference of the viewing angle of each pixel to those of channel 400 (VNIR) and channel 128 (SWIR) respectively. **(b)** and **(d)** show the angular resolution. White areas indicate channels which are excluded from evaluation due to their low sensitivity.

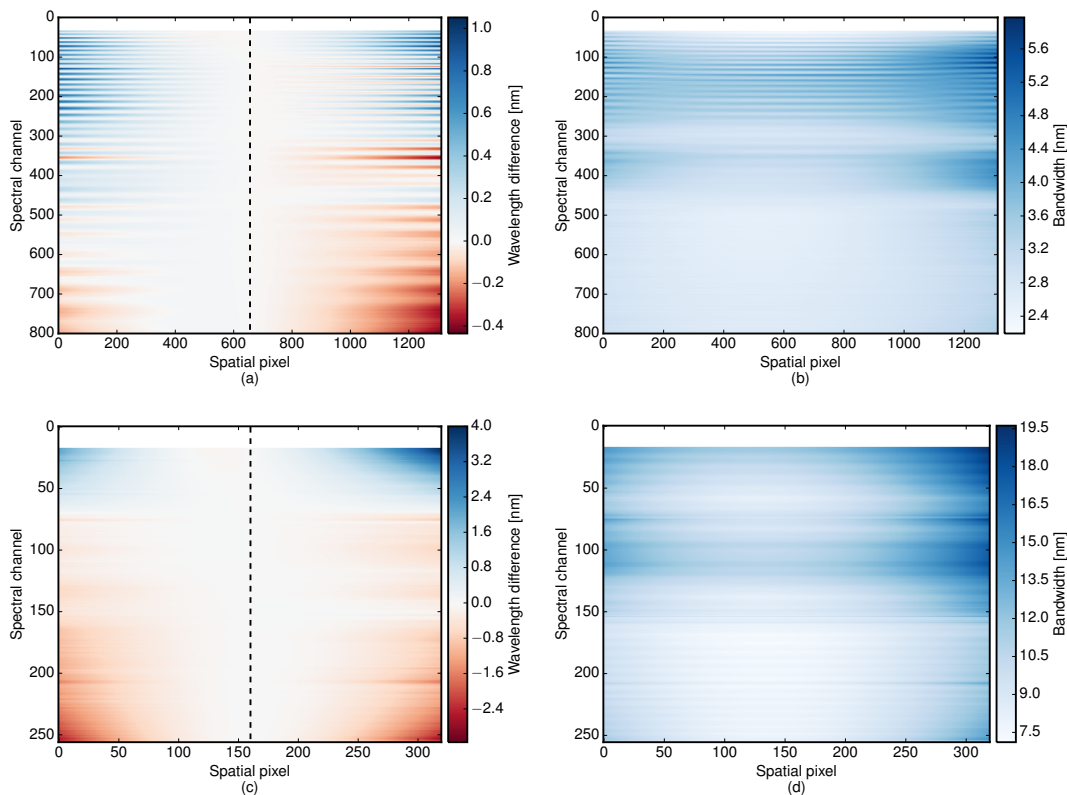


Figure 16. Spectral characterization results of the VNIR (top) and SWIR (bottom) sensor. **(a)** and **(c)** show the difference of the wavelength of each channel to those of pixel 656 (VNIR) and pixel 160 (SWIR) respectively. **(b)** and **(d)** show the bandwidth. White areas indicate channels which are excluded from evaluation due to their low sensitivity.

Design and characterization of specMACS

F. Ewald et al.

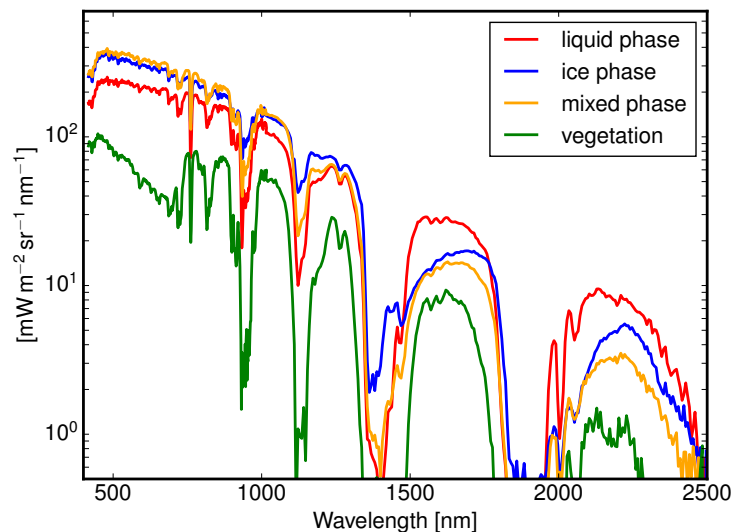


Figure 19. Reflected solar spectra measured with specMACS onboard HALO during the ACRIDICON-CHUVA campaign in Brazil.

[Title Page](#)[Abstract](#)[Introduction](#)[Conclusions](#)[References](#)[Tables](#)[Figures](#)[◀](#)[▶](#)[◀](#)[▶](#)[Back](#)[Close](#)[Full Screen / Esc](#)[Printer-friendly Version](#)[Interactive Discussion](#)

Design and
characterization of
specMACS

F. Ewald et al.

Title Page

Abstract

Introduction

Conclusions

References

Tables

Figures



Back

Close

Full Screen / Esc

Printer-friendly Version

Interactive Discussion

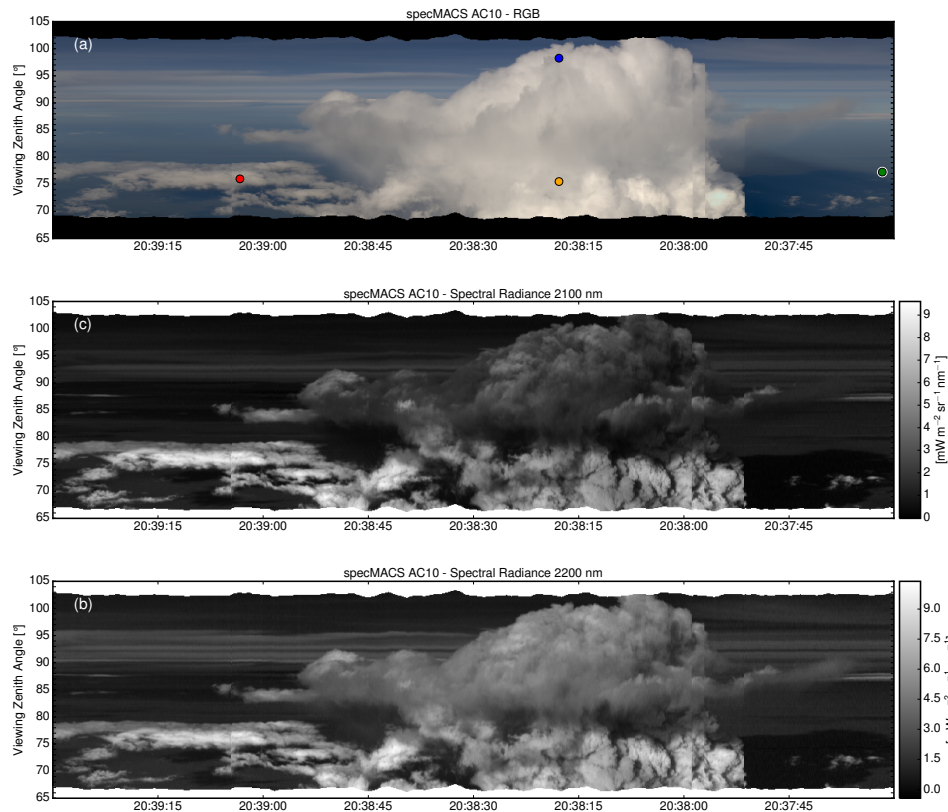


Figure 20. Spectral measurements of cloud sides taken with specMACS onboard HALO during ACRIDICON-CHUVA campaign in Brazil. **(a)** True-colour RGB calculated from the hyperspectral image, **(b)** Spectral radiance image at 2200 nm, **(c)** Spectral radiance image at 2100 nm. The ice phase is clearly visible as a distinct drop of the spectral radiances from panel **(b)** at 2200 nm to panel **(c)** at 2100 nm. The drop in radiance can be explained by the stronger ice absorption coefficient at 2100 nm compared to 2200 nm.